Protein-Lipid Interactions with Pulmonary Surfactant Using Atomic Force Microscopy

DISSERTATION

Presented in Partial Fulfillment of the Requirements for the Degree Doctor of Philosophy in the Graduate School of The Ohio State University

By

Minette Ocampo

Graduate Program in Chemistry

The Ohio State University

2014

Dissertation Committee:

Professor Heather C. Allen, Advisor

Professor Barbara E. Wyslouzil

Professor Dennis Bong

Professor Govindasamy Ilangovan

Abstract

Pulmonary surfactant is a highly surface-active lipoprotein complex that lines the alveolar surface of lungs. One of its main function is the reduction of surface tension at the alveolar air-liquid interface and prevents alveolar collapse. Surfactant protein A (SP-A) plays important functions in the promotion of pulmonary surfactant activity and phospholipid metabolism in the alveolar space and these are dependent upon the ability of SP-A to bind to the surfactant phospholipids. In the first part of the study, the binding strength of the interaction of different surfactant phospholipids, dipalmitoylphosphatidylcholine (DPPC), dipalmitoylphosphatidylethanolamine (DPPE), and dipalmitoylphosphatidylglycerol (DPPG) with SP-A is investigated using atomic force microscopy (AFM). Using AFM to measure interaction forces, the binding forces between SP-A and each of the three different surfactant lipid bilayers were measured in phosphate buffered saline (pH 7.4) with ~1 mM Ca^{2+}. For the lipid headgroup interaction with SP-A, which is assigned to the primary force value, DPPC and DPPE presented similar interaction forces while DPPG showed the weakest interaction with SP-A (*p*-value <0.001). DPPC showed the broadest distribution of forces, which was bimodal, indicating a secondary interaction resulting mainly from hydrophobic interactions of the acyl chains and choline methyl groups with SP-A. Considering the overall distribution of binding events (primary and secondary forces), DPPC revealed the strongest interaction with SP-A (headgroup and acyl chain interaction) compared to DPPE and DPPG under

dynamic conditions. Control experiments done in the absence of calcium and in the presence of SO_4^{2-} for DPPC and DPPE resulted to decrease in the unbinding forces and overall distribution of forces which can indicate partial charge neutralization of the positively charged lipid headgroup and the role of electrostatic interaction for SP-A/DPPC and SP-A/DPPE systems. SP-A/DPPG experiment done in the absence of calcium also revealed similar result which confirms Ca^{2+}-dependent binding of SP-A with DPPG.

In the second part of the study, the dissociation rate constant (K_{off}) for each SP-A/lipid systems in the presence of Ca^{2+} is experimentally calculated using the Bell-Evans model. By determining the unbinding forces at different loading rates, the unstressed K_{off} can be determined. From the calculated K_{off}s for each SP-A/lipid interaction, DPPC gave the strongest interaction among the three lipids. The dynamic force spectrum and potential energy curves revealed a two-energy barrier unbinding pathway for DPPC and DPPG while DPPE did not show a linear dependence with the loading rate. The K_{off} values obtained in this study showed weaker interactions compared to other systems used in force spectroscopy, which are mostly protein-protein systems with similar loading rates. To the best of the authors' knowledge the adhesion force and dissociation constants between SP-A and different surfactant lipids has not been reported.

Be still and know that I am God.

- *Psalms 46:10*

Acknowledgments

This thesis would have not been possible if it weren't for the help and encouragement of various people. First and foremost, I would like to thank my advisor, Dr. Heather Allen, for the support and encouragement especially when I decided to take on this project. Her guidance during my graduate studies has helped me grow as a skilled researcher. My deepest gratitude to Dr. Nadia Casillas-Ituarte for that coffee time we had that had led to this research project, for all the AFM skills and knowledge that she imparted to me and for the patience in answering my questions. To Dr. Steven Lower and Dr. Larry Schlesinger, for allowing me to use their facility and for all the valuable comments and suggestions. To Dr. Dominique Verreault, for always having time to bounce off ideas with and for all the illuminating discussions and insights. To the rest of the Allen group members, past and present, particularly Hardy Castada, Roxanna Sierra-Hernandez, Dana-Marie Telesford and Arijit Ghosh for the friendship and coffee breaks that has kept my sanity throughout these years.

To my Filipino Christian Fellowship family, for always including me in their prayers. My sincerest love and gratitude to my husband, Rex, during the last years of my graduate study especially during the dissertation process. His love, support, encouragement and understanding have sustained me and have given me that extra push

to finish my studies. To the arrival of our son, Ezekiel, who has been my motivation. To my family, for trusting and believing in me even after all the detours and even if the task seems daunting. And above all, to Almighty God, for his grace and faithfulness, who made all these possible and to whom I give back all glory, honor and praise.

Vita

September 30, 1983 .....Born – Angeles City, Philippines

2005.....B.S. Chemistry, University of the Philippines - Diliman

2011.....M.S. Chemistry, The Ohio State University

2008 to present .....Graduate Teaching Assistant, Department of Chemistry, The Ohio State University

2008 to present .....Graduate Research Associate, Department of Chemistry, The Ohio State University

Fields of Study

Major Field: Chemistry

Table of Contents

List of Tables

List of Figures

List of Abbreviations

AFM	atomic force microscopy
APP	alveolar proteinosis patient
ARDS	acute respiratory syndrome
BAL	bronchoalveolar lavage
CRD	carbohydrate recognition domain
DPPC	1,2-dipalmitoyl-*sn*-glycero-3-phosphocholine
DPPE	1,2-dipalmitoyl-*sn*-glycero-3-phosphoethanolamine
DPPG	1,2-dipalmitoyl-*sn*-glycero-3-phosphoglycerol sodium salt
GPI	glycosylphosphatidylinositol
LB	Langmuir-Blodgett
LC	liquid-condensed
MBP	myelin basic protein
PBS	phosphate-buffered saline
PC	phosphatidylcholine
PE	phosphatidylethanolamine
PEG	polyethylene glycol
PG	phosphatidylglycerol
PI	phosphatidylinositol
PS	pulmonary surfactant

PSGL-1	P-selectin glycoprotein ligand-1
RDS	respiratory distress syndrome
SEM	scanning electron microscopy
SP-A	surfactant protein-A
SP-B	surfactant protein-B
SP-D	surfactant protein-D
SLB	supported lipid bilayer
TLC	thin layer chromatography
mM	milliMolar
N	Newton
pN	pico-Newton
nN	nano-Newton
nm	nanometer
Å	Angstrom
V	volts

List of Symbols

F	Force, unbinding or rupture force
K	Cantilever spring constant
α	Deflection sensitivity
δ	Cantilever's deflection, volts
Z_c	Cantilever's deflection, nm
Z_p	Cantilever's rest position
D	Relative tip-sample distance
K_B	Boltzmann constant
z	Average value of cantilever deflection
σ	Standard deviation
X_β	Position of transition state of a single bond
r	Loading Rate
K_{off}	Dissociation rate constant
τ	Bond lifetime
K_{eff}	Effective Spring constant
υ	Cantilever retraction speed
r^2	Correlation Factor
m	Slope
b	y-intercept

Chapter 1 : Introduction

Lungs are an essential part of the respiratory system and provide the large surface area to facilitate the gas exchange needed to drive metabolic functions. The major parts of the lungs include the trachea, bronchi, bronchioles, and the alveoli. The alveoli are fluid-lined tiny air sacs in the lungs where the exchange of oxygen and carbon dioxide takes place (Figure 1.1). The average human adult has 300 million alveoli that provide a large surface area for gas exchange of up to 75 m^2.[1] The alveolus is covered by a thin-liquid lining or hypophase and the air-liquid interface is lined with a surfactant layer that is essential for the maintenance of normal lung function. Pulmonary surfactant (PS) is synthesized by alveolar Type II cells and stored in lamellar body organelles which is then secreted into the alveolar hypophase (Figure 1.2).[2,3] These lamellar bodies are then transformed to phospholipid-rich aggregates including tubular myelin. Tubular myelin is a lattice-like structure composed of phospholipid membranes in the alveolar hypophase that is believed to be an intermediate structure in the formation of surfactant monolayer from type II cells.[4,5] Lung surfactant adsorbs onto the air-hypophase interface from these aggregates to form a surfactant monolayer covering the alveolar hypophase.

A major function of PS includes the reduction of surface tension inside the alveoli to < 1 mN/m on exhalation.[2,3] This property reduces the work expenditure associated with

breathing, stabilizes the alveoli and prevents the lungs from collapsing at the end of exhalation.[2] Lung surfactant deficiency and dysfunction can lead to several respiratory diseases. Respiratory distress syndrome (RDS) is the major lung surfactant disease and is the leading cause of death of premature infants.[2] In RDS, there is insufficient production of surfactant in the lungs primarily due to lack of functional type II cells. Severe respiratory failure due to lung injury can cause acute RDS (ARDS) which occurs in all age groups. General advances in medicine have allowed the development of exogenous surfactant replacement therapy for RDS and ARDS and is still the focus of ongoing research.

PS is a lipoprotein complex that consists of ~90% lipids, ~10% proteins and small amounts of carbohydrates.[2,6,7] Phosphatidylcholines (PC) are the most abundant class of surfactant phospholipids making up ~80% of the total phospholipid.[2,7] About half of the PCs are in the form of dipalmitoylphosphatidylcholine (DPPC) which is considered to be primarily responsible for surface tension reduction of PS, thus preventing lung collapse.[7-9] The second most abundant type of phospholipids is phosphatidylglycerol (PG) which constitutes ~10% of the surfactant phospholipids.[2,7] Although the role of PG in lung surfactant processes remains unclear, recent studies have shown that it can suppress inflammatory responses in the lung.[7-10] Other lipids that are present in smaller amounts are phosphatidylethanolamines (PE) and phosphatidylinositols (PI).

The most abundant of the proteins in the lipoprotein complex is surfactant protein A (SP-A). It is a hydrophilic glycoprotein with monomeric molecular weight of 28−36 kDa, contains 228 amino acid residues and has an isoelectric point ranging from 4.8−5.2.[2,11-15] It belongs to a class of proteins known as collectins along with surfactant protein D (SP-D). SP-A is an octadecamer consisting of six trimeric subunits. Each subunit consists of four domains: an amino-terminal domain, a collagen-like domain, an alpha helical coiled-coil neck domain, and a Ca^{2+}-dependent carbohydrate recognition domain (CRD) (Figure 1.3).[13,16] The primary structure of SP-A is shown in Figure 1.4. The amino terminal is a short peptide segment of 7 amino acids with a cysteine residue which forms an interchain disulfide bridge. The collagen-like domain is composed of 73 amino acids consisting of 23 repeating glycine-X-Y tripeptide units where Y is often hydroxyproline.[13,17,18] After the 13th Gly-X-Y triplet, an interruption occurs as a result of the insertion of a proline residue and the substitution of a cysteine for a glycine that introduces a flexible kink in the collagen region causing each trimeric subunit to bend outward and gives rise to the "flower-bouquet like" structure of SP-A.[13,17,18] The neck and the CRD region are composed of 148 amino acid residues.[17] The neck region consists of a short sequence of hydrophobic residues and amphipathic helix and the CRD contains a Ca^{2+}-dependent carbohydrate binding site which may play a role in pathogen recognition and clearance, and lipid aggregation.[13,19-21]

SP-A is secreted by alveolar type II cells into the alveolar space and is shown to be associated with the surfactant phospholipids.[11] Numerous studies have investigated the

lipid-binding properties of SP-A using various biochemical and biophysical methods and under different experimental conditions such as temperature, pH and the amount of calcium that can affect the lipid binding properties of SP-A. Various methods have been employed such as centrifugation,[22,23] resonant mirror spectroscopy,[24,25] infrared spectroscopy,[26] and electron microscopy[27,28] to study SP-A binding with phospholipid bilayers using multilamellar or unilamellar vesicles. Lipid monolayer studies have also been done with SP-A.[29,30] SP-A/lipid binding has also been observed using thin layer chromatography (TLC) by immobilizing the lipids on silica gel to observe direct binding of labeled SP-A.[31]

Although several studies have shown the role of Ca^{2+} in inducing phospholid vesicle aggregation,[32-35] there have been contradictory reports however on the Ca^{2+} dependence binding of SP-A with lipids. Kuroki and Akino reported Ca^{2+}-dependent binding of I^{125}-SP-A with DPPC adsorbed on silica gel.[31] King et al. demonstrated that the binding of SP-A to DPPC vesicles occurs in the presence of EDTA when the vesicles are in the gel phase.[22] Fluorescence studies have revealed increase in the intrinsic fluorescence of SP-A when DPPC vesicles are in the gel phase.[36] These studies indicate that SP-A/DPPC binding is dependent on the physical state of the vesicle and is independent on Ca^{2+}. Studies on DPPC monolayers showed that the presence of Ca^{2+} in the subphase did not affect the properties of SP-A/DPPC films but improved the miscibility of SP-A with DPPG films and DPPC/DPPG films.[15,30] Previous lipid binding studies suggest that SP-A binds to both the headgroup and acyl chains of phospholipids in a Ca^{2+}-dependent

manner.[24,25,31,32,36] Mutagenesis studies have also shown that the phospholipid binding domain of SP-A overlaps with the CRD and that the latter affects its lipid binding properties and aggregation.[37-41] The alpha helical coil neck region in SP-A may also contribute to lipid binding and may be involved in phospholipid uptake of various cells.[42,43]

Among other functions, SP-A also enhances the surface tension lowering properties of phospholipids and modulates the secretion, uptake, and recycling of surfactant.[13,44] The continuous clearance of surfactant from the alveolar hypophase is important in maintaining the steady state condition in the lungs.[44] Alveolar type II cells and macrophages play a role in the recycling and degradation of surfactant, respectively.[44,45] The process of selective targeting of specific classes of surfactant by these two types of cells is still unclear. However, studies have shown that SP-A enhances the uptake of lipids by alveolar type II cells and macrophages through the activation of macrophages and its binding to putative SP-A receptors.[45-48] SP-A also facilitates the formation of tubular myelin in a Ca^{2+}-dependent manner in vitro and has been shown to interact with ordered lipids in membranes of interfacial films.[25,30,36,49] These functions are dependent on the ability of SP-A to interact with the certain types of surfactant lipids.

In this work, the lipid binding properties of SP-A to different surfactant phospholipids (DPPC, DPPE, and DPPG) was investigated using AFM. AFM has been widely used in biology to study ligand-receptor interactions because of its high

sensitivity. [50] Binding or adhesion forces can also be employed to study different cell-cell or cell-substrate interactions.[50-53] Additionally, AFM has the ability to characterize the interactions between phospholipids and proteins under dynamic conditions. The ability of AFM to measure protein-lipid binding was shown by Desmeules et al. wherein they measured a binding force of ~48 pN between recoverin, a Ca^{2+}-myristoyl switch retinal protein, and a supported DPPC bilayer.[54] Cross et al. also employed AFM-based force spectroscopy to determine the binding force between glycosylphosphatidylinositol (GPI)-anchored alkaline phosphatase protein and supported DPPC bilayer wherein they measured ~350 pN binding force.[55] The interaction of SP-D with different saccharide ligands was also studied using AFM by Thormann et al. who measured binding forces in the range of 35−55 pN binding.[56] To the best of the authors' knowledge the adhesion force between SP-A and different surfactant lipids has not been reported.

The work presented in this dissertation can provide insight on the selective SP-A/lipid interactions in the alveolar hypophase under dynamic conditions. Using force spectroscopy, the lipid binding properties of SP-A are investigated allowing better and detailed understanding on the interaction forces and binding mechanism involved in the interaction of SP-A with the different surfactant lipids.

In Chapter 2, AFM theory and principles are introduced and force spectroscopy is discussed in detail. Chapter 3 presents the materials and methods used in this study. Chapter 4 presents the work on the measurement of the binding forces of SP-A with the

different surfactant lipids (DPPC, DPPE and DPPG) using AFM. DPPC and DPPE presented similar headgroup interactions with SP-A while DPPG showed the weakest interaction. DPPC showed a bimodal and the broadest distribution of forces that suggest strong interaction with SP-A. The differences and origin of the binding forces for each SP-A/lipid systems is discussed. The determination of dissociation rate constant (K_{off}) for each SP-A/lipid systems is presented on Chapter 5. The unbinding forces at different loading rates were measured and plotted using the Bell-Evans model to generate a dynamic force spectrum. The K_{off} was then calculated and results revealed a stronger interaction of SP-A with DPPC. The potential energy curves were also plotted for each interaction to reveal the energy landscape of the unbinding pathway for each SP-A/lipid systems.

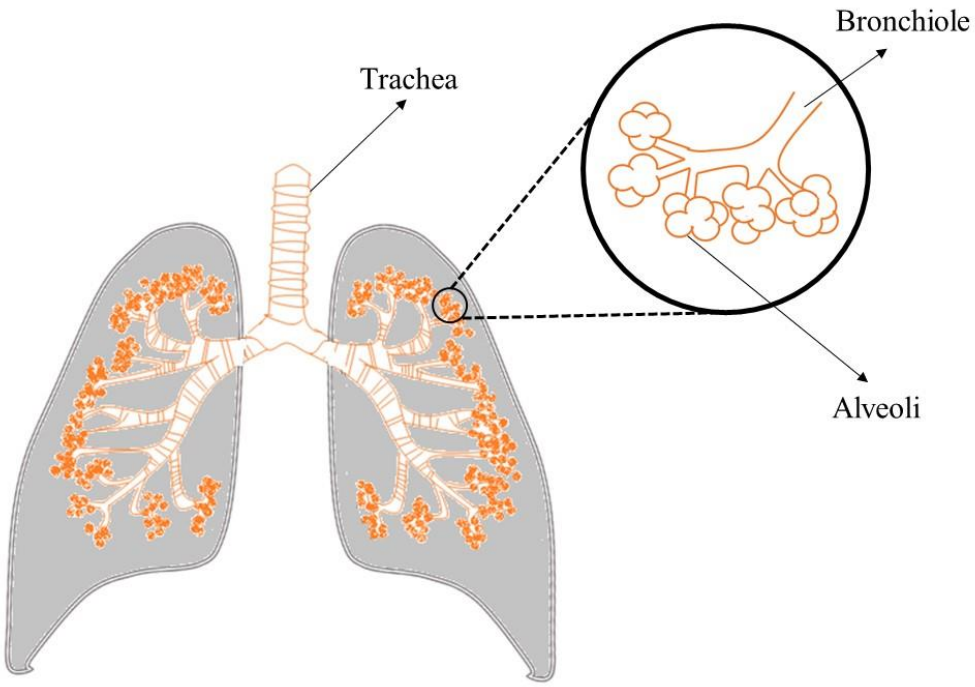

Figure 1.1 Diagram of the lungs. The mammalian lungs branch into tubes leading to tiny air sacs called alveoli where oxygen and carbon dioxide gaseous exchange takes place. The lungs contain hundreds of millions of alveoli with diameters ranging from 75–300 μm in adults.

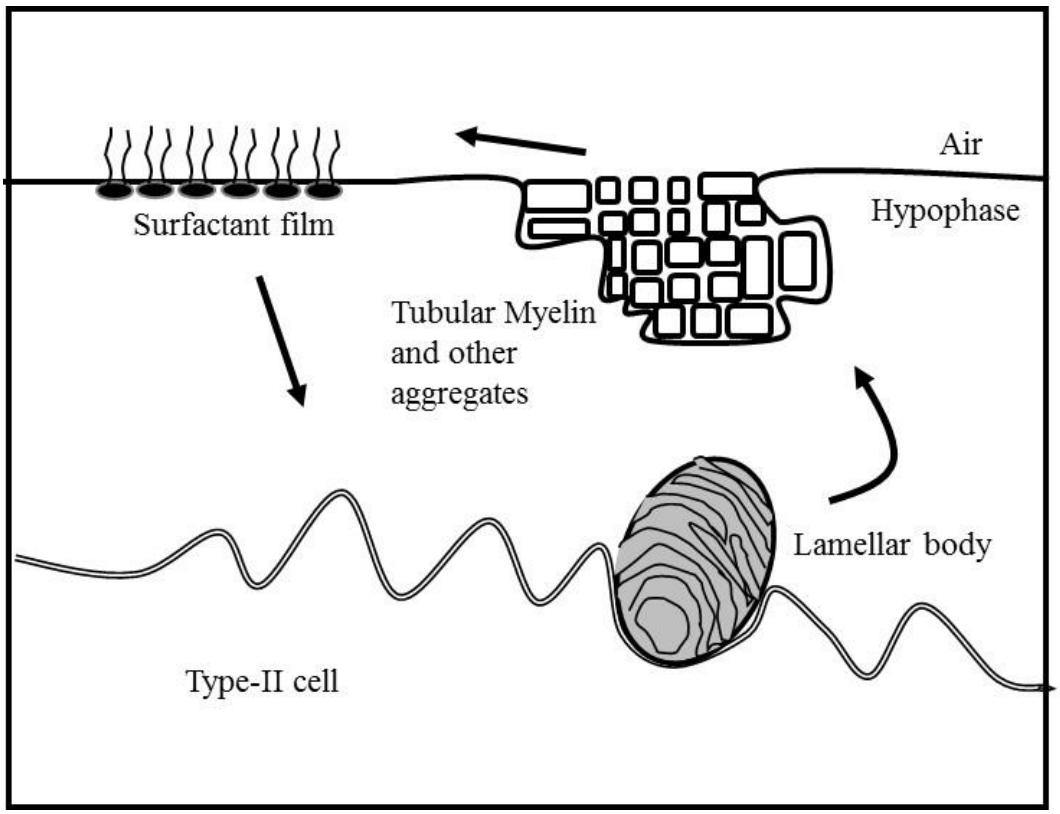

Figure 1.2 Schematic overview of the pulmonary surfactant system. Lung surfactant is synthesized, secreted and recycled by the alveolar type II cell. It is stored in lamellar bodies and secreted to the alveolar hypophase which then forms tubular myelin and other aggregates. Lamellar bodies and tubular myelin both contains the lipoprotein components of surfactant. The lung surfactant from these aggregates then adsorbs to form a film at the air-liquid interface. The surfactant in the hypophase is then taken back to the Type II cell for recycling. (Adapted from Notter, 2000)[2]

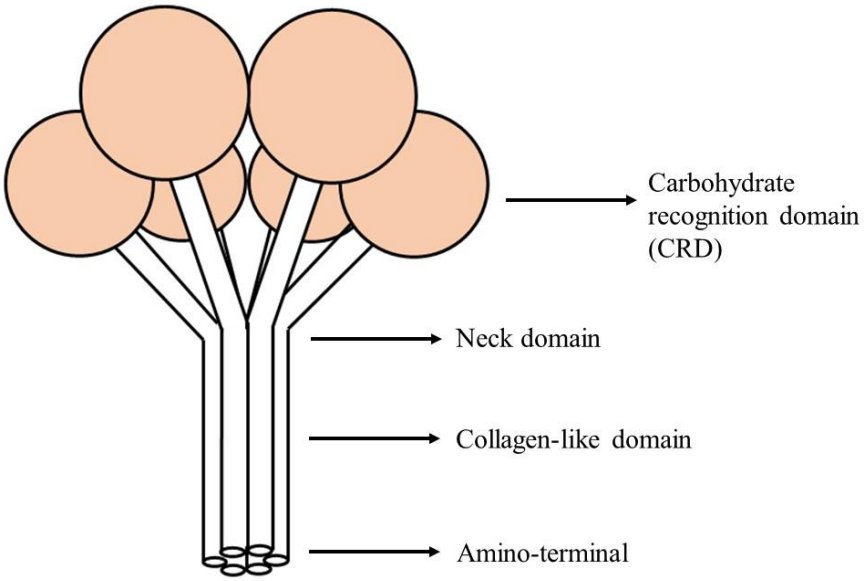

Figure 1.3 Structure of SP-A. SP-A consists of six trimeric subunits that forms an octadecamer with a "flower bouquet-like" structure. The primary structure consists of an amino-terminal domain, a collagenous domain, a neck domain, and a carbohydrate-recognition domain (CRD). SP-A is the most abundant of the pulmonary surfactant proteins and is relatively hydrophilic.

N-terminal Domain

Glu-Val-Lys-Asp-Val-Cys-Val-

Collagen-like Domain

Gly-Ser-Pro-Gly-Ile-Pro-Gly-Thr-Pro-Gly-Ser-His-Gly-Leu-Pro-Gly-Arg-Asp-Gly-Arg-Asp-Gly-Leu-Lys-Gly-Asp-Pro-Gly-Pro-Pro-Gly-Pro-Met-Gly-Pro-Pro-Gly-Glu-Met-Pro-Cys-Pro-Pro-Gly-Asn-Asp-Gly-Leu-Pro-Gly-Ala-Pro-Gly-Ile-Pro-Gly-Glu-Cys-Gly-Glu-Lys-Gly-Glu-Pro-Gly-Glu-Arg-Gly-Pro-Pro-Gly-Leu-Pro-

Neck Domain

Ala-His-Leu-Asp-Glu-Glu-Leu-Gln-Ala-Thr-Leu-His-Asp-Phe-Arg-His-Gln-Ile-Leu-Gln-Thr-Arg-Gly-Ala-Leu-Ser-Leu-Gln-Gly-Ser-

Carbohydrate Recognition Domain

Ile-Met-Thr-Val-Gly-Glu-Lys-Val-Phe-Ser-Ser-Asn-Gly-Gln-Ser-Ile-Thr-Phe-Asp-Ala-Ile-Gln-Glu-Ala-Cys-Ala-Arg-Ala-Gly-Gly-Arg-Ile-Ala-Val-Pro-Arg-Asn-Pro-Glu-Glu-Asn-Glu-Ala-Ile-Ala-Ser-Phe-Val-Lys-Lys-Tyr-Asn-Thr-Tyr-Ala-Tyr-Val-Gly-Leu-Thr-Glu-Gly-Pro-Ser-Pro-Gly-Asp-Phe-Arg-Tyr-Ser-Asp-Gly-Thr-Pro-Val-Asn-Tyr-Thr-Asn-Trp-Tyr-Arg-Gly-Glu-Pro-Ala-Gly-Arg-Gly-Lys-Glu-Gln-Cys-Val-Glu-Met-Tyr-Thr-Asp-Gly-Gln-Trp-Asn-Asp-Arg-Asn-Cys-Leu-Tyr-Ser-Arg-Leu-Thr-Ile-Cys-Glu-Phe

Figure 1.4 Primary structure of SP-A. The 228 amino acid sequence is derived from cDNA by Floros et al.[57] and White et al.[58] and is taken from Notter[2]. The secondary structures of the neck and carbohydrate recognition domain are also specified according to Head et al.[59]. Blue residues form coiled structures, red residues form alpha helix and green residues form beta strand structures.

Chapter 2 : AFM Theory

2.1 Atomic Force Microscopy

Atomic force microscopy (AFM) is a high resolution imaging technique based on the measurement of attractive and repulsive interaction forces between a cantilever tip and a sample surface. It was invented on 1986 by Binnig and Quate[60] wherein they demonstrated for the first time the theory of AFM, which uses an ultra-small probe tip at the end of the cantilever. The AFM technique is based on the interaction between a sharp probe attached to a flexible cantilever and a sample at a very short probe-sample distance (0.2−10 nm).[61] The main contributions to the attractive forces are Van der Waals force, electrostatic force, and short range chemical force.[62] The repulsive forces in general are very short-range forces and include Pauli-exclusion repulsion and electron-electron Coulomb interactions.[62] For AFM imaging, the image contrast arises because of the forces present between the tip and the sample which is a function of the tip-sample distance and the material of both the tip and the sample.

In topographic measurements, the AFM tip is scanned over the sample surface while maintaining a constant interaction force between the tip and the sample. The cantilever deflects in the *z*-direction due to the surface topography of the sample, and depending whether the tip-sample interaction is attractive or repulsive, the cantilever will deflect towards or away from the surface (Figure 2.1). The vertical and lateral deflections of the

cantilever are measured using the optical lever. The optical lever operates by focusing and reflecting a laser beam off the rear of the cantilever. The reflected laser beam strikes a four-quadrant photodetector which indicates the position of the laser spot on the detector and the angular deflections of the cantilever. The output from the photodetector controls the force applied to the tip so that the force remains constant. A feedback loop is used to regulate the force applied on the sample. The feedback loop consists of a tubular piezoelectric device that controls the height of the cantilever, tip and optical lever which measures the height of the sample. The feedback circuit keeps the cantilever deflection constant by adjusting the voltage applied to the scanner.

AFM provides a 3D profile of the sample surface with sub-nanometer scale resolution. For imaging, the resolution depends strongly on the shape of the tip. The smaller the tip, the smaller the surface area sampled by the tip, hence a better imaging resolution. The most common type of AFM tips are made of silicon nitride (Si_3N_4) and are pyramidal and conical in shape with a radii of ~20-60 nm.[61] Si_3N_4 tips have very low force constants and is also known as a low-wear material, thus minimizing tip wear and distortion of AFM data.[63,64]

2.2 Modes of AFM

Depending on the distance of the tip and the sample surface different operating modes are possible for AFM. Generally, AFM has three imaging operating modes: the contact mode, non-contact mode, and tapping mode (Figure 2.2). In all these three

modes, the tip is scanned across the sample surface and the topography of the sample is obtained by interpreting the cantilever deflection.

2.2.1 Contact Mode

In the contact mode or constant force mode, the tip is in permanent physical contact with the sample. The cantilever's deflection signal is maintained at a set point value via an electronic feedback loop. The image of the surface topography is created by measuring the deflection of the cantilever required to maintain a constant force. Contact mode AFM is appropriate for hard and stable materials since the tip is in close contact with the sample. The shear forces applied to the sample while scanning may damage soft materials with weakly bound molecules. In the contact region, at a very small tip-sample distance, repulsive forces predominate due to the overlap of the electronic orbitals at atomic distances. Typical forces applied to contact mode AFM are in the order of nN.

2.2.2 Non-Contact Mode

In non-contact mode, the AFM probe is brought into close proximity to the sample surface and senses the long-range attractive forces (Van der Waals forces) that induce a frequency shift in the resonant frequency of the cantilever. In this mode, the tip oscillates at the resonance frequency and the amplitude of the oscillation is kept constant using a feedback loop during scanning. This method is most suitable for soft materials since the tip never actually touches the surface resulting in low deformation and shear

forces on the sample. The greatest drawback of this mode is that it cannot be used in liquid environment because this can interfere with the oscillation.[65]

2.2.3 Tapping Mode

The AFM tapping mode uses an oscillating tip. During the oscillation, the tip is brought into contact with the sample so that the forces felt by the tip are the same as that in the contact mode. The contact time however is greatly reduced in this mode and since the tip is not in contact with the sample during lateral movement while scanning, shear forces applied to the sample is negligible and this prevents the tip from sweeping the molecules on the surfaces. This mode provides better lateral and vertical resolution than contact and non-contact mode and can be used in liquid environment.

2.3 Force Spectroscopy Mode

Although AFM is best known for its high resolution imaging capabilities, it can also be a powerful tool for sensitive force measurements. Forces in the piconewton (pN) range can be measured which is the order of magnitude of forces that are required to separate receptors from ligands. The small radius of the AFM tip allows a small interaction area and high sensitivity for smaller forces. In AFM imaging mode, the cantilever is usually scanned over the sample surface to generate a 3D image. In force spectroscopy, the cantilever-tip assembly acts as a sensitive force sensor. The cantilever and the tip are moved towards the sample in the *z*-direction while maintaining the *x*-*y* position of the AFM probe fixed. The tip approaches the sample until it is contact with it

and then retracted again, while the interaction between the tip and the sample is measured. This is then repeated several times at the same spot and different locations to give a better statistical understanding of the interaction. AFM can directly measure the force between the atoms or molecules at the end of the probe and the surface. Often, the ligand is immobilized on the AFM tip and the receptors immobilized on the surface. The presence of interaction forces causes the cantilever to deflect and the deflections of the cantilever are recorded which gives rise to force-distance curves or briefly "force curves".

Force curves provide quantitative information of interaction forces present between the tip and the sample by measuring the amount of force felt by the cantilever as the tip approaches the sample surface. Figure 2.3 shows the movement of the cantilever during the force spectroscopy experiment and the corresponding force curve generated. During the approach phase, at position (1) which is about 10−100 μm away from the sample, there is no tip-sample contact. As the cantilever approaches the sample surfaces, at several microns away from the sample, long-range interactions, such as electrostatic interactions can be measured. At position (2), at nanometers away from the sample, short-range forces, such as Van der Waals or capillary forces, can be measured. At this distance, when the sum of the forces is attractive, the tip may jump into contact with the surface. Once the cantilever is in contact with the surface, the cantilever deflects further due to increasing force as the cantilever is pushed towards the sample and this gives rise to the linear part of the force curve (position 3). At this point, the stiffness and elastic

response of the sample can be measured. The cantilever then retracts in the *z*-direction and force felt by the cantilever decreases. Adhesion forces keep the tip in contact with the sample and this leads to a negative deflection of the cantilever and results to a negative peak in the force curve (position 4). The cantilever then breaks free from the surface and returns to its starting deflection.

The result of a force measurement is a measure of the cantilever deflection in volts (V) versus the displacement of the piezo element in nm. The force **F** between the tip and the sample is related to the cantilever's deflection through Hooke's law:[63,66]

$$F = K\alpha\delta \tag{2-1}$$

where K is the cantilever's spring constant (N/nm), α is the deflection sensitivity (nm/V) and δ is the measure cantilever's deflection in volts (V).

The piezo element displacement (Z_p) defines the distance between the sample surface and the rest position of the cantilever. Z_p has to be converted to the relative tip-sample distance D (nm) by taking into account the cantilever deflection in nm (Z_c). D is calculated by the piezo element displacement corrected by the deflection of the cantilever (Figure 2.4):

$$D = Z_P - Z_C \tag{2-2}$$

Force-distance curve then is a plot of the force versus the true tip-sample distance calculated from the raw data.

2.4 Regions in the Force Curve

The approach and withdrawal curves can be divided into three regions: the contact region, non-contact region, and the zero line (Figure 2.5). The zero line is obtained when the tip is far from the sample, such that there is no tip-sample contact and the cantilever's deflection is close to zero. As the tip is moved and pressed against the surface, the corresponding cantilever deflection is called the contact region and can provide information on the sample stiffness.[61] The non-contact region of the approach curve gives information about attractive or repulsive forces present at this certain tip-sample distance. When the overall force felt by the cantilever is attractive, this will result to pull-on forces (jump-to-contact) and if it is repulsive, this will give rise to a positive peak on the curve. The non-contact region in the withdrawal curve contains the jump-off contact due to pull-off forces as the tip is retracted from the surface. This pull-off force is the adhesion force that exists between the tip and the sample.

2.5 Tip Functionalization

AFM adhesion experiments are based on the interaction between two molecules: one attached to the AFM tip and the other bound to the surface. Tip functionalization with the molecule of interest is an important strategy in the force spectroscopy experimental

design. Employing the appropriate functionalization techniques would lead to more significant and reliable results. Bare tip-sample adhesion is often observed but this is often referred to as a nonspecific interaction. The challenge in every experiment is finding a way to distinguish between the desired or relevant interaction from nonspecific interactions and background noise. One important step to accomplish this goal is choosing the appropriate attachment strategy. There are numerous considerations that influence the choice of functionalization method, the practicality of the method and the type of system being probed would often dictate the choice.

The most commonly used method for attachment is the use of intermediate molecules, called spacers or linkers, between the tip and the molecule of interest. Most commonly used spacers are short polyethylene glycol (PEG) polymer chains.[67] This method provides the molecule with flexibility and mobility to best access the binding receptor on the surface. Although this method provides a simple way of functionalizing the tip and providing the molecule with spatial freedom to interact with the receptor, this configuration always requires extensive controls to distinguish between the specific and the nonspecific interactions. Nonspecific interactions in this case can arise from the interaction of the spacer or linker with the receptor and can make analysis of force measurements complicated.

Although there are other approaches of tip functionalization, basic issues must always be addressed in choosing the best attachment strategy. One must choose an

appropriate AFM probe. Oftentimes, the most important consideration is the spring constant. For binding experiments, typically the spring constants used are < 0.1 N/m (soft cantilevers) because the forces measured for binding interactions are usually small.[68] The use of a linker or spacer must also be considered if it will provide more benefits in promoting and recognizing specific binding events. Appropriate experimental conditions for tip functionalization and force measurement must also be ensured to maintain the integrity and binding activity of the molecules of interest.

2.6 Calibration

The cantilever's spring constant, *K*, is oftentimes estimated by the manufacturer and a more accurate calibration method can be done to determine the spring constant. One of the popular methods that is used for calibration and is used for this study is the thermal tune method. This method involves measuring the cantilever's mechanical response to thermal fluctuations including the diffusion of small particles (Brownian motion). The end position of the cantilever is constantly fluctuating because of the thermal vibrations from the environment. The size of the fluctuations is measured by the AFM system by measuring the cantilever's vertical deflection over some time and these vertical deflections are then analyzed. The thermal noise spectrum is a plot of the cantilever's fluctuations as a function of frequency. The greatest amplitude is usually seen around the cantilever's resonance frequency. The noise spectrum is then fitted with a Lorentzian function and an estimate of the spring constant can be measured.

This method was first presented by Hutter et al.[69] Due to the small deflections in the cantilever, the method assumes the cantilever has a single degree of freedom and follows the equipartition theorem. The theorem states that for a system in thermal equilibrium, the average energy in any free mode of the system has to be equal to $K_BT/2$, where K_B is the Boltzmann constant and T is the absolute temperature.[69,70] The energy in the resonance is given by the spring constant, K, and the average value of the vertical deflection of the cantilever, z:[71]

$$\frac{1}{2}K_BT = \frac{1}{2}K < z^2 > \quad (2\text{-}3)$$

The value of z^2 is taken from the Lorentzian fit of the thermal noise spectrum by taking the area under the curve which corresponds to the energy in the resonance. For most commercial AFMs, calibration is done through their software.

2.7 Noise

The limits of force sensing and force resolution in AFM are determined by the overall noise in the system. Noise introduced in AFM measurements can arise from both internal and external sources. Internal sources of noise are primarily due to thermal vibrations of the cantilever when it is in contact with air or liquid.[67] External sources of noise include mechanical and acoustic vibrations and the turbulence in the liquid environment. Both sources of noise can limit the force resolution. The noise determines the lower limit of force that the AFM can detect. The noise level of a force-distance

curve due to these sources is usually ≤30pN.[66] But with the improvement in commercially available cantilevers, forces down to ~10pN can be measured.[72]

Along the zero line (no tip-sample contact), the noise is dominated by thermal vibrations. To minimize the effect of thermal drift, force measurements should be done at high scan rates but still at a certain threshold speed before dynamic effects affect the measurements.[66] Acoustic noise can be minimized by using an appropriate enclosure. Active vibration isolation stages are also employed for isolation solutions. Systematic errors can also arise in the calculation of forces through the inaccurate estimation of the cantilever spring constant. The estimation of distances can also be affected by systematic errors due to the piezo response, hysteresis and creep.

2.8 Statistics

The number of force curves that must be taken for a force measurement experiment depends on several factors. Not all force measurements will give the binding interaction of interest. Either no interaction will be sensed (no binding event in the force-distance curve) or non-specific interactions will be measured which are mixed with measurements that show specific interaction. Collecting a large number of force curves can then allow one to still have a significant number of specific binding events after filtering the non-desired force curves. For complicated systems, such as the existence of multiple bonds, the standard deviation can become large, requiring more force measurements to accurately determine the mean.

In general, from the statistics of normally distributed data, the number of samples that should be acquired, n, so that the true mean lies within a margin of error E with a confidence defined by z* is given by:

$$n = (\frac{z^* \sigma}{E})^2 \tag{2-4}$$

where σ is the standard deviation and the z^*-score for 99% confidence is 2.576. For large loading rates, the standard deviation for the distribution of rupture forces is $\sigma = \frac{K_B T}{X_\beta}$ where X_β is the position of the transition state of a single bond.[73,74] This equation shows that few measurements are actually needed to estimate the mean rupture force. If the objective of the experiment is to find the mean of the unbinding forces, this can be done with relatively fewer samples than those required to accurately fit the distribution to a histogram of the forces measured. However, to analyze the data beyond the estimation of the mean force and to resolve finer details in the force histogram, then larger number of samples is needed.

2.9 AFM Applications

AFM has proven to be a suitable approach for the study of wide variety of samples (conductors and insulators) and may be operated in various environments such as in vacuum, air or liquid. This makes AFM particularly suited for biological applications

because the samples can be imaged in physiological conditions. In its imaging mode, it provides a three-dimensional topographical information with sub-nanometer resolution providing quantitative height information. Its super resolution is its main advantage over optical microscopy and scanning electron microscopy (SEM). Also, compared to SEM, the samples need not be electrically conductive or dehydrated which allows probing of the sample nondestructively and in its hydrated state. AFM have been used in the high resolution imaging of different samples such metals, polymers, biomolecules, bio-membranes and cells.[75-82]

One of the major advantage of AFM is that it provides information on some local mechanical properties and interaction forces through the analysis of force-distance curves. AFM has been successfully employed in the study of various ligand-receptor interaction[83-86], polymers and DNA.[87,88]

2.10 Determination of Dissociation Rate Constant

An external mechanical force applied to a system can deform the energy landscape of the unbinding path and shortened the bond lifetime significantly below its natural lifetime. Figure 2.6 shows how an increasing force can change the energy landscape and lower the activation barrier. In 1978, Bell emphasized the increase in rate of bond dissociation under external force.[89] In his model, he predicted that the unbinding force of a ligand-receptor bond should depend logarithmically on the loading rate:

$$F = \frac{K_B T}{X_B} \ln\left(\frac{r X_B}{K_{off} K_B T}\right) \quad (2\text{-}3)$$

where F is the most probable value for the rupture force, r is the loading rate which is a measure of the rate at which force is applied to the system. It can be determined as the product of slope of the rupture event (pN/nm) and the tip's retraction speed (nm/s). K_{off} is the dissociation constant in the absence of the applied force. By plotting the average unbinding force vs. the loading rate and extrapolating to zero force, K_{off} can be estimated. The value of K_{off} provides insight into the dynamics of the interaction, strength of the bonds and the bond relaxation time ($\tau = 1/K_{off}$).

A plot of the unbinding force vs. the logarithm of the loading rate usually gives rise to a straight line (Figure 2.7). For an energy landscape with a single barrier, this would give rise to a simple linear force spectrum (Figure 2.7A). For systems involving more than one barrier, this will lead to multiple linear regimes in the force spectrum plot (Figure 2.7B). Each linear regime corresponds to the overcoming of s single energy barrier along the unbinding pathway. For a system with more than one energy barrier, and assuming all barriers lie along a single unbinding pathway, the spectrum is predicted to follow a continuous sequence of linear regimes.[50,90] By varying the loading rate of the force applied, one can make different barriers emerge and can map the dissociation landscape of the system. This can provide detailed insight on the molecular dynamics of a ligand-receptor system.

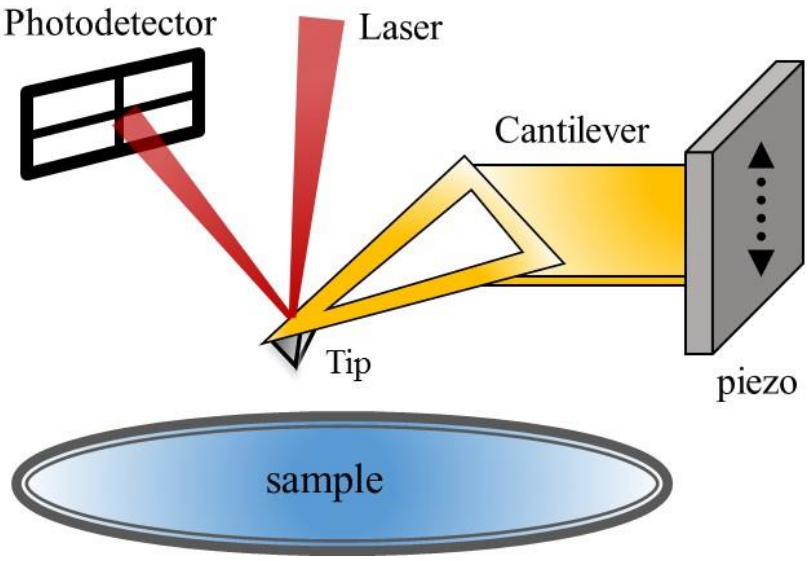

Figure 2.1 Schematic of a tip-scanning atomic force microscope. The tip, which is mounted on a cantilever with a specific spring constant, is scanned over the sample surface. While scanning, the force between the tip and the sample is measured by monitoring the deflection of the cantilever with a four quadrant photodiode using an optical lever sensor. In an optical lever, a laser beam is focused on and reflected from the rear of the cantilever. A small deflection of the cantilever causes a large change in the laser spot position at the detector.

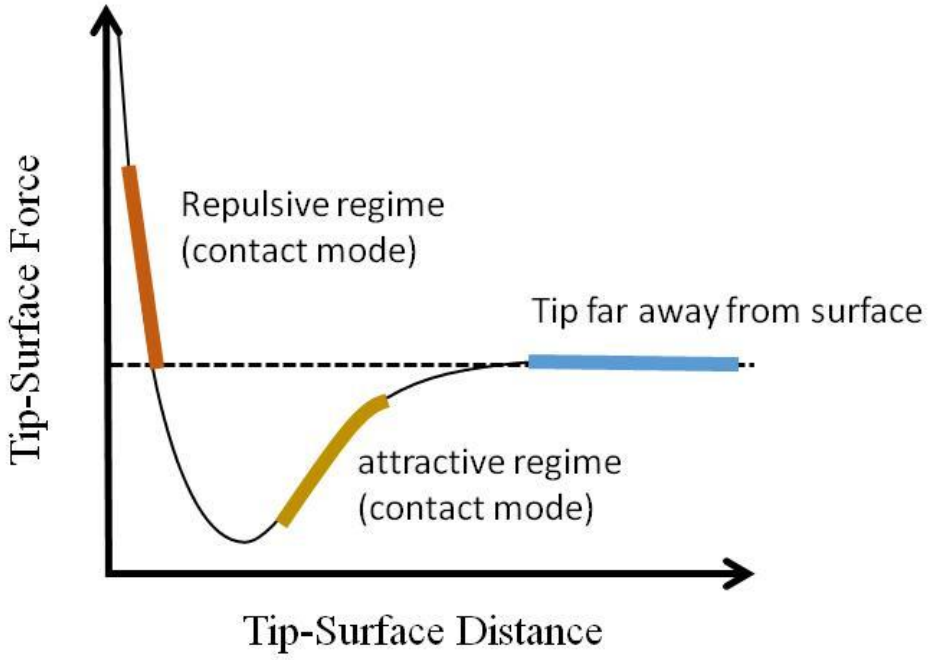

Figure 2.2 Interatomic force vs. distance curve.

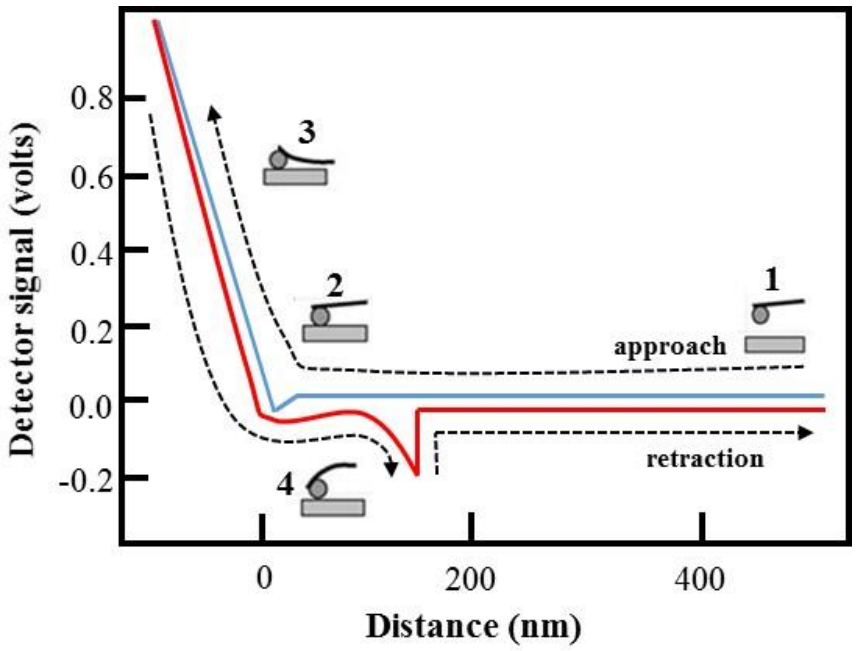

Figure 2.3 Example of a force-distance curve. During the approach phase, there is no tip-sample contact (1). As the tip approaches the sample, the tip may jump into contact with the sample surface (2) due to Van der Waals and electrostatic forces. The cantilever deflects further due to increasing force and gives rise to the linear part of the curve (3). The tip then retracts in the z-direction and the force of the cantilever is decreasing. Adhesive forces present between the tip and the sample keep the tip in contact with the sample and leads to a negative deflection of the cantilever (4). The tip then breaks free from the surface (pull-off force) and returns to its starting position.

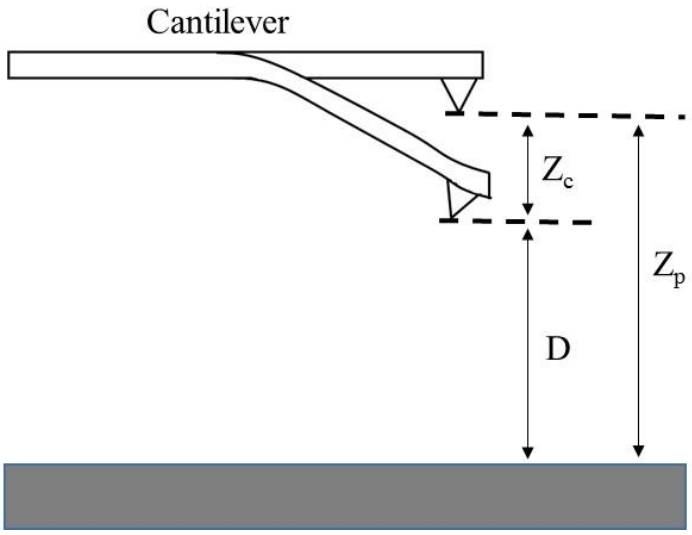

Figure 2.4 The tip-sample distance. *D* is the actual tip-sample distance and *Zp* is the distance between the rest position of the cantilever and the sample surface and is the distance controlled during measurement. Interaction forces present causes cantilever deflection (Z_c) and this changes the actual distance between the cantilever and the sample surface.

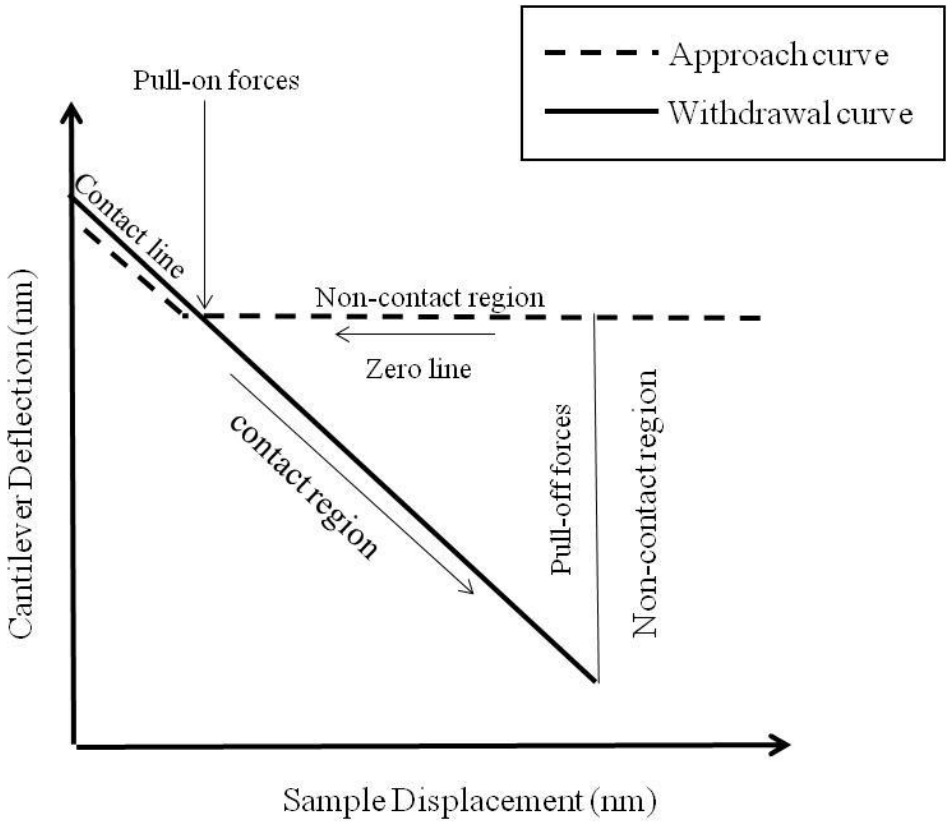

Figure 2.5 Regions in the force-distance curve (adapted from Leite and Herrmann, 2005).[91]

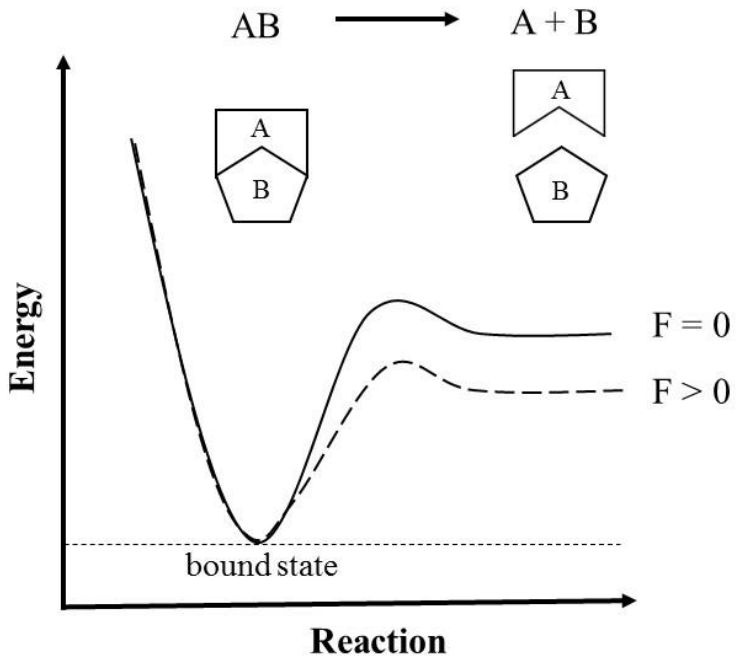

Figure 2.6 A schematic diagram of the energy landscape illustrating the dissociation in the absence of external force (solid line) and with an applied force (dashed line). The schematic shows how an external mechanical force deforms the energy landscape by reducing the barrier of the unbinding path.

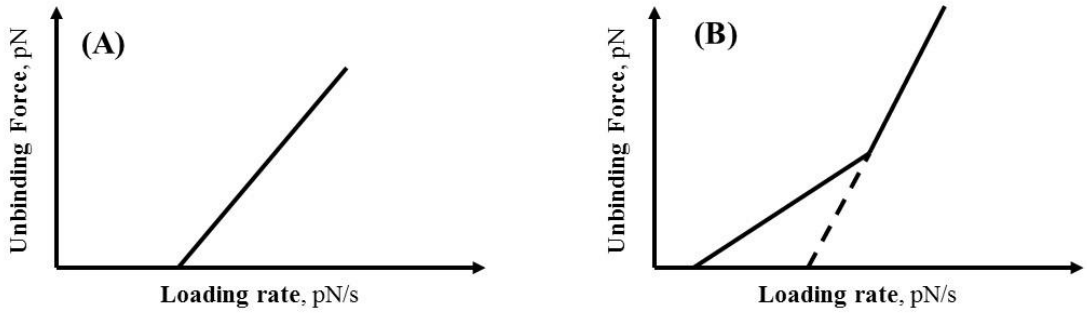

Figure 2.7 Dynamic force spectra. The unbinding force usually scales linearly with the logarithm of the loading rate. For a single barrier, the plot of unbinding force vs. the logarithm of the loading rate is a simple linear force spectrum (A). For a system involving two barriers that lie along a single unbinding pathway, this is predicted to follow a continuous sequence of linear regimes in the force spectrum (B). (Adapted from Lee et al., 2007)[50]

Chapter 3 : Experimental Materials and Methods

3.1 Materials

All synthetic lipids (purity >99%), namely 1,2-dipalmitoyl-*sn*-glycero-3-phosphocholine (DPPC), 1,2-dipalmitoyl-*sn*-glycero-3-phosphoethanolamine (DPPE), and 1,2-dipalmitoyl-*sn*-glycero-3-phospho-(1'-rac glycerol) (DPPG) were purchased from Avanti Polar Lipids (Alabaster, AL) and used as received. Molecular structure of lipids used are shown in Figure 3.1. Spectrophotometric grade chloroform and methanol were purchased from Fisher Scientific. Nanopure water with a resistivity of 17.9 MΩ·cm was obtained from a Barnstead Nanopure filtration system with a measured pH of 5.5. Phosphate-buffered saline (PBS) solution (pH 7.4) with and without cations was purchased from Life Technologies (Grand Island, NY). PBS solution with cations contains ~0.9 mM $CaCl_2$ and ~0.5 mM $MgCl_2$. Triangular DNP-10 silicon nitride (Si_3N_4) AFM tips were purchased from Bruker (Camarillo, CA) with a nominal spring constant of 0.06 N/m.

3.2 Lipid Solutions Preparation

1 mM DPPC solution was prepared by dissolving DPPC in chloroform. 1 mM DPPG and DPPE solutions were prepared in a chloroform: methanol mixture of 3:1 (v/v) and 2:1(v/v), respectively.

3.3 Purification of SP-A

Bronchoalveolar lavage (BAL) from alveolar proteinosis patients (APP) was used to obtain APP-SP-A.[92] SP-A preparation was assessed by SDS-PAGE with 99% purity. Bacterial endotoxin levels were determined using the *Limulus* amebocyte lysate kit (BioWhittaker, Walkersville, MD). Endotoxin levels in SP-A preparations ranged from undetectable to 0.2 pg/μg protein. Two SP-A functional assays, oxidative burst and liposome aggregation,[93,94] were performed as quality control experiments.

3.4 AFM Tip Preparation and Functionalization

AFM tips were UV-cleaned for 10 min and then coated with the protein by immersion of the cantilever in a ~25 μg/ml solution of SP-A in PBS for 1 h at ~37°C. The tip was then carefully rinsed with PBS to remove loosely bound protein and was used immediately for AFM measurements.

3.5 Langmuir Blodgett Technique

The Langmuir-Blodgett (LB) technique allows the fabrication of highly ordered organic films.[95] An LB film contains one or more monolayers of the organic material deposited onto a solid substrate by immersing the substrate in the liquid. A Langmuir trough is the equipment used for the production of LB films (Figure 3.2). It consists of a container that is made from an inert material such as Teflon that holds the liquid subphase onto which the monolayer is spread. The barriers, equipped with a position detector to measure the film's surface area, allow symmetric film compression to a

certain surface pressure that is measured by a surface area sensor. Langmuir troughs used for the fabrication of LBs are made with dipping wells for the immersion of solid substrates. By successively dipping the solid substrate up and down through the monolayer and keeping the surface pressure constant, the monolayer at the air-liquid interface (Langmuir monolayer) is adsorbed onto the substrate and allows the formation of highly organized multilayer films. Generally, to ensure formation of a homogenous film, the deposition is done at high surface pressure to ensure sufficient cohesion in the monolayer.

In this study, the supported lipid bilayers (SLBs) were prepared using the LB method with a Minimicro LB-trough from KSV Instruments (Monroe, CT). A lipid monolayer was first formed by spreading the lipid solution at the air-water interface at 25°C. After 10 min to allow the solvent to completely evaporate, the barriers were compressed at a constant speed of 5 mm/min to the liquid-condensed (LC) phase corresponding to a surface pressure of 40 mN/m for DPPC and 30 mN/m for both DPPG and DPPE. [96] The monolayer was then allowed to equilibrate for 10 min and the surface pressure was continuously monitored and kept constant during the deposition process by the Wilhelmy plate method. The LB film was then generated by a single downstroke on a clean glass slide at a rate of 1 mm/min through the air-monolayer interface. The second layer was then transferred by a single upstroke at the same speed. The freshly formed SLBs were kept in a Petri dish containing a small amount of water to ensure hydration prior to AFM

measurements. To maintain the integrity of the SLB during the AFM measurements, force curves were collected within 5 h after bilayer preparation.

3.6 AFM Force Spectroscopy

All force measurements were performed on a Dimension Icon atomic force microscope (Bruker, Camarillo, CA) (Figure 3.3). It is a tip-scanning AFM wherein the probe is raster-scanned over the sample surface to monitor probe-sample interactions. It utilizes an XYZ closed loop head that scans at high speed rates with low drift and low noise. It is also equipped with a high resolution camera to efficiently locate and focus the sample and for faster probe positioning.

Force-distance curve measurements were conducted in PBS solution with and without the presence of Ca^{2+} at ambient temperature. Figure 3.4 shows the schematic for the experimental setup for force measurements. The functionalized tip is mounted on the AFM probe and allowed ~10 min to equilibrate in the buffer solution before performing the calibration with Nanoscope software (v. 8.10) using the thermal tune method[69] to determine an accurate value of the spring constant. The software allows the in-situ analysis of the thermal noise and automatic spring constant calculation without the need of any extra equipment. Experimental spring constants of the cantilevers used for each lipid were measured to be 0.08 ± 0.01 N/m. The force-distance curves were generated by bringing the protein-functionalized tip towards the SLB at a loading rate of ~5.55 μm/s and then retracting it while recording the unbinding forces. This approach-retraction

cycle is then repeated several times at five different locations on the SLB to obtain >300 force curves per location. For each set of curves only the final rupture peak was considered for the unbinding force values.[97-100] These values were then analyzed statistically to obtain the force distribution (histogram), which was then fitted with a multi-Gaussian function (Origin 8.0, OriginLab, Northampton, MA) as previously reported.[54-56] The unbinding force distribution for each protein-lipid system is the average of the measurements performed at different locations on the lipid bilayer and with different cantilevers on at least three different protein-lipid systems. The distribution profile then serves as an indicator of the binding properties of SP-A to the different lipids.

3.7 Dynamic Force Spectrum

The dynamic force spectra in this study are generated by determining the rupture force and loading rates of >500 force curves for each protein-lipid systems. The rupture force is determined by taking the difference between the peak and the baseline (Figure 3.5). The effective spring constant (K_{eff}) is obtained by determining the slope of a straight line fit to the curve before the point of bond rupture (Figure 3.5). For this study, the K_{eff} is obtained using the scanning probe image processor (SPIP) software (version 5.1.11). The K_{eff} is then used to determine the loading rate (described in detail on Chapter 5). For a group of data points, the mean loading rate is obtained along with the most frequent unbinding force within that group. For each average loading rate and most frequent unbinding force the standard deviations are determined. These data points are

then plotted to generate the dynamic force spectrum with the standard deviations for the error bars.

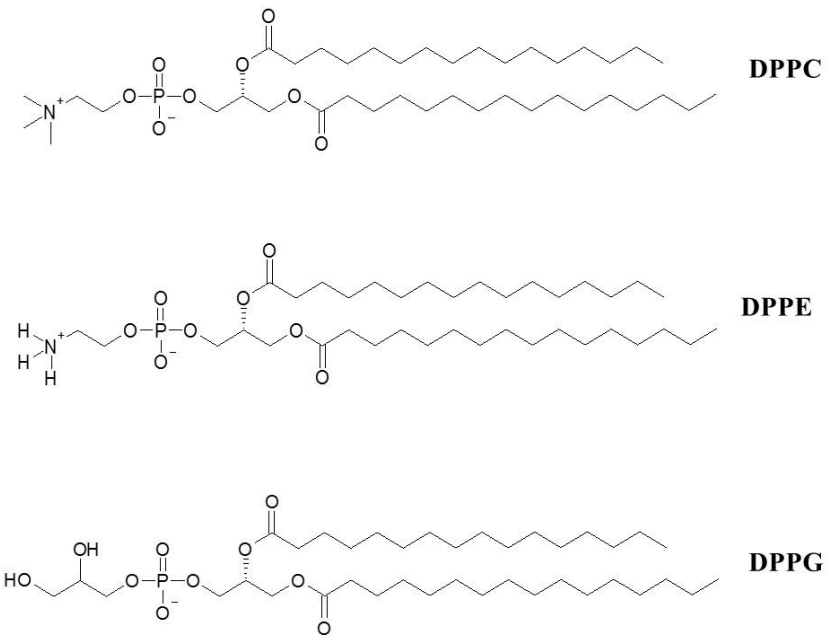

Figure 3.1 Molecular structures of the studied phospholipids.

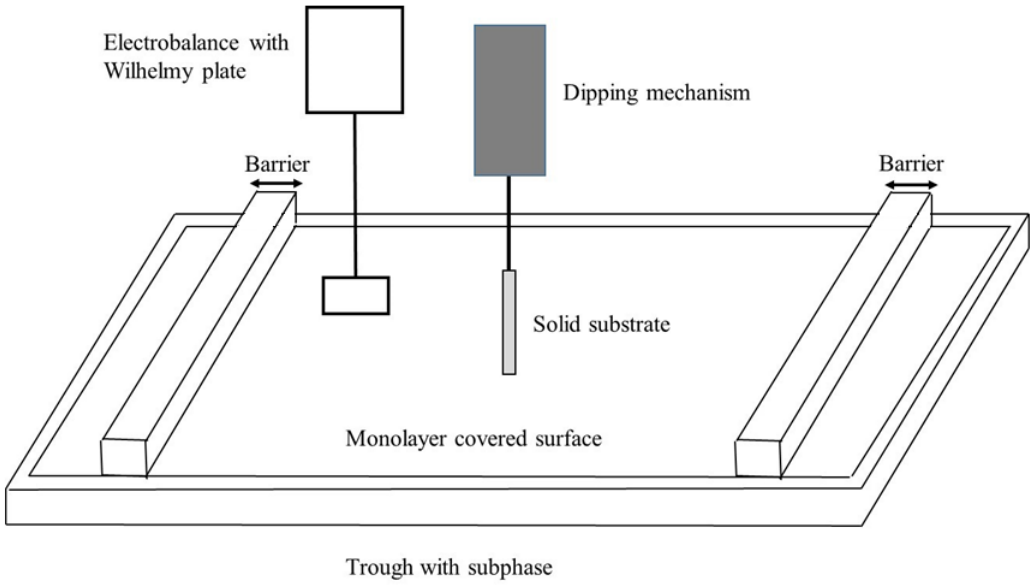

Figure 3.2 Schematic illustration of a Langmuir trough with a Wilhelmy plate balance to measure surface pressure and moveable barriers for symmetric compression or expansion. For the fabrication of LB films, a dipping mechanism is included to hold the solid substrate as it is immersed into the liquid.

Figure 3.3 The atomic force microscope used for this study at the Surface Analysis Laboratory of the Department of Chemistry and Biochemistry at The Ohio State University.

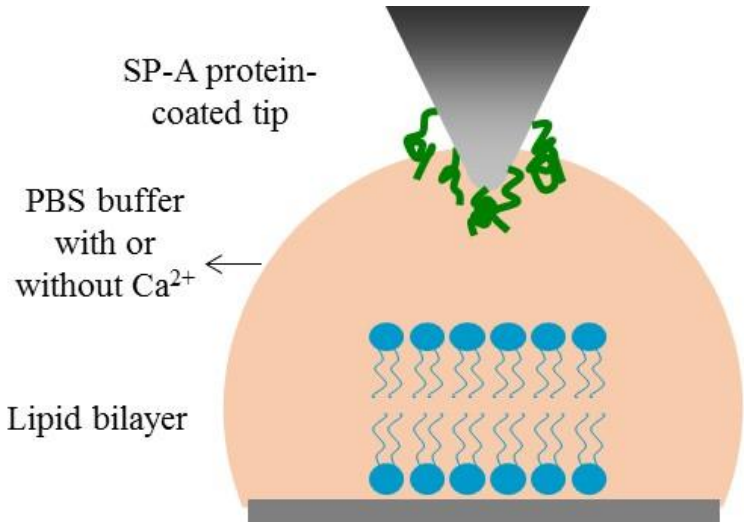

Figure 3.4 Experimental setup for force measurements.

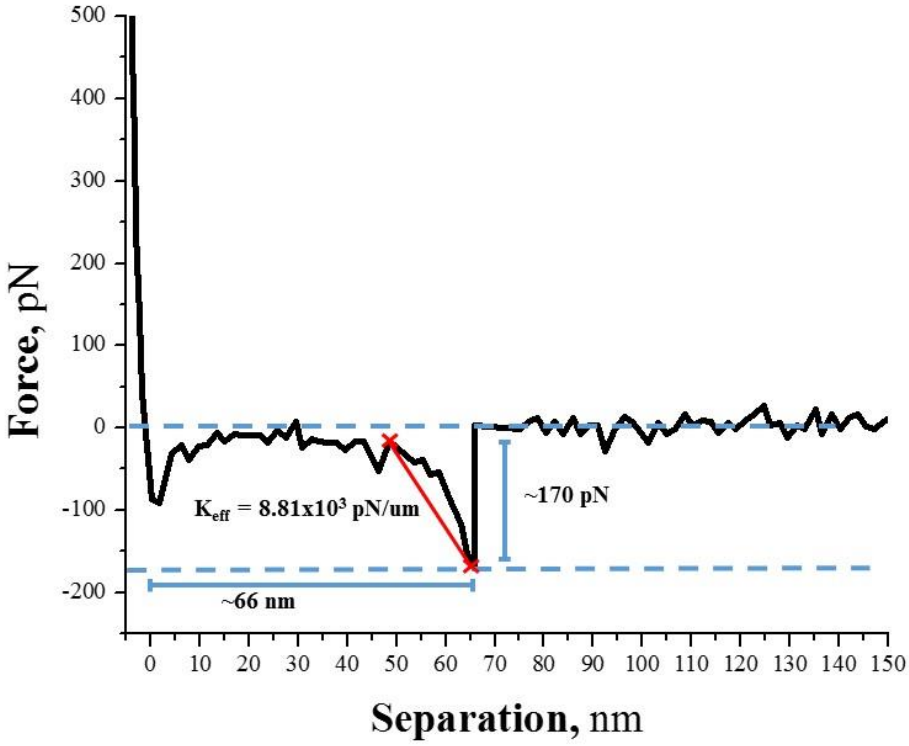

Figure 3.5 Representative force-distance curve from AFM measurements. From the force-distance curve, the unbinding force (*F*), the separation distance (*D*) and the effective spring constant (K_{eff}) can be extracted.

Chapter 4 : Determination of Binding Strengths for Each Protein-Lipid Systems

4.1. SP-A/Lipid Interactions in the Presence of Ca^{2+}

In the work presented here, the lipid headgroup interaction with SP-A in the presence of Ca^{2+} was investigated. This interaction may be important in SP-A's role in lipid aggregation and in its association with ordered membranes in the gel-like phase and with lipid vesicles. To assess this interaction, SLBs of surfactant lipids with identical acyl chains, but with different headgroup charge (at neutral pH, DPPC and DPPE are zwitterionic, while DPPG is negatively charged) were studied.

The binding affinity of SP-A for the three different surfactant lipids was determined. In these experiments, the SP-A-functionalized AFM tip was brought into contact with each SLB allowing the protein to interact with the lipid headgroups and/or acyl chains (Figure 4.1). The AFM tip was then retracted while the unbinding force between the SP-A and the SLB was measured. This procedure was repeated at different locations of the SLB to ensure a homogeneous examination of the sample. Most locations revealed a significant number of force curves that showed binding events while few locations showed low binding frequencies, mostly generated force curves with no interaction detected. The low binding frequencies are possibly due to inhomogeneity of the lipid bilayer film or the presence of lipid packing defects. AFM imaging studies of lipid

bilayer have shown that a low surface pressure deposition leads to more lipid packing defects.[101-103] In this study, deposition was done at high surface pressure to ensure a homogenous bilayer and minimized lipid packing defects. Freshly prepared bilayer films were also used to ensure integrity of the film. This was demonstrated by Cross et al, wherein an AFM image of a freshly prepared DPPC bilayer film deposited at ~40mN/m showed a smooth morphology compared to a week-old DPPC bilayer that revealed numerous dark regions or holes in the AFM image (Cross).[55] In these binding studies, >8000 force curves were collected from samples prepared from different protein extraction procedures and different lipid bilayers.

Figure 4.2 shows representative force curves for the SP-A/DPPC interaction that revealed unbinding events. Force curves (i) and (ii) had similar rupture lengths but different magnitudes of unbinding force, while force curve (iii) presented a longer rupture length but similar unbinding force as (i). Force curve (iv) showed the longest rupture length and the largest unbinding force. Physically, this means that the protein is adhering more strongly to the bilayer compared to the interaction in (i)-(iii). Similar force curves as those shown in Figure 4.2 were obtained for the SP-A/DPPG and SP-A/DPPE systems. The differences in the rupture length can also arise from the unfolding of a portion of the protein due to the retraction process. Aside from multiple binding, protein unfolding can also contribute to multiple peaks in the force-distance curve, thus, the peak that describes the largest separation distance is considered for the unbinding force as mentioned in the Experimental Methods (Chapter 3). Figure 4.3 is an example of a force curve that shows

multiple peaks. For such force curves, the peak furthest out (largest separation distance) is considered as the unbinding event.

The distributions of the unbinding forces for the three different SP-A/lipid systems are shown in Figure 4.4. Table 4.1 shows the average peak force for each SP-A/lipid interaction deduced from the multi-Gaussian fit. The unbinding strength between SP-A and the three surfactant lipids follows in the order of DPPC ≈ DPPE > DPPG. DPPC and DPPE interactions with SP-A produced primary force values of ~80 pN. The fact that DPPC and DPPE showed comparable peak unbinding force with SP-A suggests that the nature of the lipid headgroup plays an important role in the interaction with SP-A. As mentioned above, both DPPC and DPPE headgroups are zwitterionic at neutral pH. The primary unbinding force is therefore assigned to electrostatic interactions of the dipolar zwitterionic headgroups with SP-A. In contrast, DPPG generated the weakest interaction among the three lipids with SP-A with a force of ~70 pN. DPPG is negatively charged resulting in weaker electrostatic interactions with SP-A as the overall surface charge of SP-A is also negative at pH 7.4.[11]

Although the majority of the unbinding forces of SP-A with DPPC and DPPE resulted in similar force values, DPPC presented a bimodal and broader force distribution, indicating the presence of secondary interactions of DPPC with SP-A (Figure 4.4A). A stronger bimodal character was also observed in the force distribution of the SP-A/DPPG system, suggesting that both DPPC and DPPG have two types of

interaction with SP-A. The relatively large unbinding forces measured for the second mode of DPPC (~160 pN) and DPPG (~250 pN) are assigned to interactions of the multiple binding sites of SP-A with the lipid bilayer.[11] Another cause for the larger forces measured could be the presence of hydrophobic interactions arising from the partial penetration of SP-A into the DPPC and DPPG lipid bilayers.

The packing of the lipids in the SLBs may account for the differences in unbinding forces observed among the three surfactant lipids. For instance, DPPE is known to form a more packed and ordered bilayer relative to DPPC due to the smaller size of the DPPE headgroup and the ability of DPPE to interact via intermolecular H-bonding.[104-106] This can also be observed from the surface-area isotherms of each lipid in water at room temperature (Figure 4.5). The LB films for each lipid were taken at 40 mN/m for DPPC and 30mN/m for DPPG and DPPE, all in the LC phase. At these surface pressures, the isotherm of DPPE is shifted to a lower mean molecular area compared to DPPC and DPPG indicating a more packed and densed monolayer in the LC phase. The closer packing of the DPPE bilayer could restrict the penetration of SP-A and minimize hydrophobic interactions with the lipid acyl chains. DPPG, however, does not have the ability to create such intermolecular H-bonds,[104] and for this reason, SP-A can penetrate more easily into the bilayer, thereby resulting in increased hydrophobic interactions. This behavior has also been seen with myelin basic protein (MBP) which is believed to interact hydrophobically with lipid fatty acid chains. To this point, MBP showed less binding with PE than PG, which is consistent with weaker hydrophobic interactions

caused by closely packed PE molecules.[107,108] In the case of DPPC, not only can the DPPC zwitterionic headgroup contribute to electrostatic interactions with SP-A, but the methyl groups of the choline headgroup can also provide sites for hydrophobic interactions. These additional hydrophobic interactions could be responsible for the larger unbinding forces. Our findings are consistent with previous studies of the SP-A/DPPC system which suggest that the principal mode of DPPC interaction with SP-A is hydrophobic in nature and that the hydrophobic neck domain of SP-A may contribute to its lipid binding property.[31,33,37,43,59]

Other studies have also revealed stronger interactions of SP-A with DPPC compared to other surfactant phospholipids. ^{125}I-SP-A binding to lipids immobilized on TLC silica plates indicated that SP-A specifically binds to DPPC in the presence of Ca^{2+} ions.[31] Other reports did not show specificity but observed preference of SP-A to bind with DPPC and weaker binding affinities with other surfactant phospholipids.[15,25,30,33] In the work presented here, considering the overall force distribution (primary and secondary interactions) for each SP-A/lipid system, DPPC gave the broadest distribution and thus the largest average unbinding force among the three lipids. This average force accounts for the overall strength of interaction of SP-A with DPPC and takes into account the headgroup and acyl chain contributions in the interaction with SP-A. This broad distribution of unbinding forces can be a rationale for the preferred and stronger interaction of SP-A to DPPC.

It is important to mention that the results given in the current work were obtained under dynamic conditions due to the mechanical stress applied to the system, whereas all previously reported SP-A/lipid binding studies were conducted under equilibrium conditions. In dynamic force spectroscopy, the bond dissociation is a stochastic process and is dependent upon the nature of the interaction and the magnitude of the force applied to the system.[51,56] As mentioned above, the main unbinding force is assigned to the SP-A/lipid headgroup interaction. The unbinding force values found here were similar for DPPC and DPPE which somewhat contradicts a previous SP-A binding assay study conducted under equilibrium conditions wherein the PC headgroup showed preference over PE and PG.[25] This deviation is most likely due to the dynamic conditions of the experiment, the orientation of the protein and the lipids, and how they are supported on a solid substrate.

As mentioned by Thormann et al., working in the dynamical regime constitutes a more representative model of the interaction of SP-A with the surfactant lipids in the alveolar hypophase.[56] SP-A can experience shear forces in its interaction with lipids due to the expansion and contraction of the pulmonary alveoli during breathing. SP-A may also be bound to the surface of type II cells and macrophages[45-48] and may not be free in solution when interacting with lipids. This is similar to this work's experimental setup wherein SP-A is bound to the AFM tip. It should also be mentioned that the magnitude of the forces measured in this study may change using a different loading rate. Under dynamic conditions, the unbinding force for weak bonds is dependent upon the force that

is applied.[51] In this experiment, the relative strength of unbinding forces for the three lipid-systems was investigated thus the same loading rate was used to compare the results under the same conditions.

4.2. Control Experiments

The magnitude of the binding forces and their frequency distribution are indicators of the specificity of the interaction among the three different lipids with SP-A. To further test the specificity of the interaction, control experiments were conducted (Figure 4.6). The control experiments involved blocking the binding sites of SP-A with a ligand such as surfactant lipids in buffer solution. Initially, in the absence of a ligand, an SP-A-coated tip was brought into contact with a DPPC bilayer in buffer, and force curves were collected. The initial buffer was then replaced with a buffer containing ~1 mM DPPC to partially block the lipid binding sites of SP-A and additional force curves were then collected. DPPC showed strong interaction with SP-A and can thus effectively block the binding site of the protein. After the addition of 1 mM DPPC, only 26% of the total force curves showed specific binding events. When ~10 mM DPPC was used to block the binding sites, a further decrease of binding frequency to 12% was observed. A significant reduction in binding frequency after lipid addition is observed, confirming the specificity of the probed interaction. The reduction in frequency showed to be statistically significant after addition of 1 mM DPPC (p-value < 0.0025) and after addition of 10 mM DPPC (p-value < 0.0001). The decrease in the binding frequency of the control experiments can be attributed to the partial blocking of the lipid binding sites

of SP-A at this lipid concentration. Since the critical micelle concentration (cmc) for DPPC in aqueous solution is ~10^{-10} M, [2,109] the DPPC in buffer solution used in this blocking control experiment is composed mostly of lipid vesicles and not free lipids in solution. However, these lipid vesicles can still bind to the lipid binding domain of SP-A and affect the binding ability of SP-A with the lipid bilayer.

Additional control experiments were conducted by probing the interaction of a bare tip with each lipid bilayer and the interaction of a SP-A coated tip with glass slide. A binding frequency of <3% was observed for each bare tip–lipid system and ~5% for a SP-A coated tip and glass interaction. These binding frequencies are significantly less than the binding frequencies (>15%) observed for an SP-A/lipid system. This reduction in frequency also confirms the specificity of the SP-A/lipid interaction.

Initial experiments were also performed on DPPC and DPPG using carboxymethylcellulose, a linker, to tether SP-A on the AFM tip through its N-terminal group and subsequently have its C-terminal end free to interact with the lipid bilayer. These results show a higher overall unbinding force for DPPC when compared with DPPG. Control experiments (i.e. without SP-A), however, showed a significant contribution of nonspecific interactions from the linker to the overall unbinding force between the protein and the lipid bilayer. Therefore, to avoid any force contributions from the linker, all subsequent experiments were conducted without it. Even in the case without the linker, DPPC showed a higher unbinding force relative to DPPG. Moreover,

it is likely that the orientation of SP-A with and without the linker is similar as evidenced by the comparable differences in the SP-A/lipid unbinding forces.

4.3. SP-A/Lipid Interactions in the Absence of Ca^{2+}

Additional control experiments were done in the absence of Ca^{2+}. For the SP-A/DPPC and SP-A/DPPE interaction however, SO_4^{2-} was added to the PBS solution to probe the screening effects of the positive charge of the lipid headgroup. Prior studies have shown the role of Ca^{2+} in lipid binding of SP-A.[11] There have been contradictory reports however on the Ca^{2+}-dependent binding to DPPC. For instance, Kuroki and Akino reported the Ca^{2+}-dependent binding of ^{125}I-SP-A with DPPC.[31] Meyboom et al. obtained similar results with DPPC/egg-PC/PG/cholesterol liposomes.[24,31] In contrast, other studies revealed no direct influence of Ca^{2+} on the binding of SP-A to DPPC. The presence of Ca^{2+} ions in the subphase did not change the properties of the SP-A/DPPC monolayer films and fluorescence studies showed no Ca^{2+}-dependent binding of SP-A to DPPC vesicles.[15,36]

In these control experiments, the SP-A/DPPC and SP-A/DPPE systems were investigated in the absence of Ca^{2+} and in the presence of a divalent anion (1 mM SO_4^{2-} in PBS buffer) to test the contribution of the positive charge of the DPPC and DPPE headgroup on the main unbinding force through electrostatic interactions. Figures 4.7A and 4.7B show the distribution of the unbinding forces for DPPC and DPPE in the presence of SO_4^{2-}, respectively. There is a decrease in the unbinding forces for DPPC (~73 pN, 5% decrease) and DPPE (~67 pN, 15% decrease) in the presence of the anion

which can indicate the partial charge neutralization of the positively charged lipid headgroup. DPPE's amine headgroup is less shielded compared to DPPC's choline headgroup allowing efficient interaction of SP-A with the positively charged amine, resulting in a significant decrease in the unbinding force relative to DPPC when SO_4^{2-} is present. There is also a decrease in the overall distribution of forces as compared to Figures 4.4A and 4.4B which suggests a minimized multiple binding and decreased hydrophobic interactions. This decrease in the unbinding forces due to partial charge neutralization suggests the contribution of electrostatic interactions for the DPPC/SP-A and DPPE/SP-A systems.

In the case of DPPG, the presence of Ca^{2+} was shown in a previous study to promote SP-A/DPPG interactions. The presence of Ca^{2+} improved the ability of SP-A to mix with DPPG and DPPC/DPPG monolayers and a decrease in the interaction of DPPC/DPPG vesicles with SP-A was observed in the absence of Ca^{2+}.[15,36] In this control experiment, as discussed above, due to the negative charge of DPPG, the SP-A/DPPG interaction resulted in a lower unbinding force than DPPC and DPPE indicating a weaker interaction with SP-A. The presence of Ca^{2+} however can partially neutralize the charge of DPPG and increase interaction with SP-A. To confirm the role of Ca^{2+} in the promotion of SP-A interaction with DPPG, the SP-A/DPPG system was probed in the absence of Ca^{2+}. There was a decrease in the main unbinding force (~60 pN, 13% decrease) for the SP-A/DPPG system as shown in Figure 4.7C. There was also a decrease in the overall unbinding force as evidenced by the decrease in the distribution of the unbinding forces

as compared to Figure 4.4C. The decrease in the main unbinding force and the overall distribution of force indicates the Ca^{2+}-dependent binding of SP-A to DPPG.

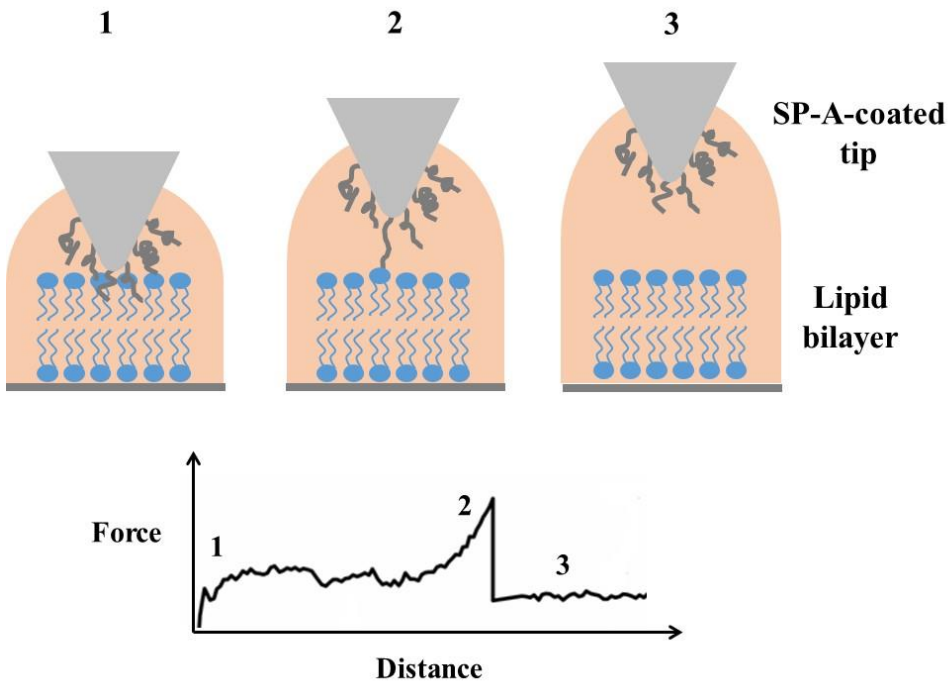

Figure 4.1 Illustration of the experimental setup for the interactions between the SP-A-functionalized AFM tip and the SLB in PBS buffer. The AFM tip is incubated with SP-A solution and the lipid bilayer is supported on a glass slide. The tip is moved directly towards the sample (1) then retracted (2) and if adhesion forces are present, a positive peak is generated in the force-distance curve. The tip is then continuously retracted until the interaction between the protein and the bilayer is ruptured (3). A force curve is then generated which provides quantitative information of the forces present between the SP-A and bilayer.

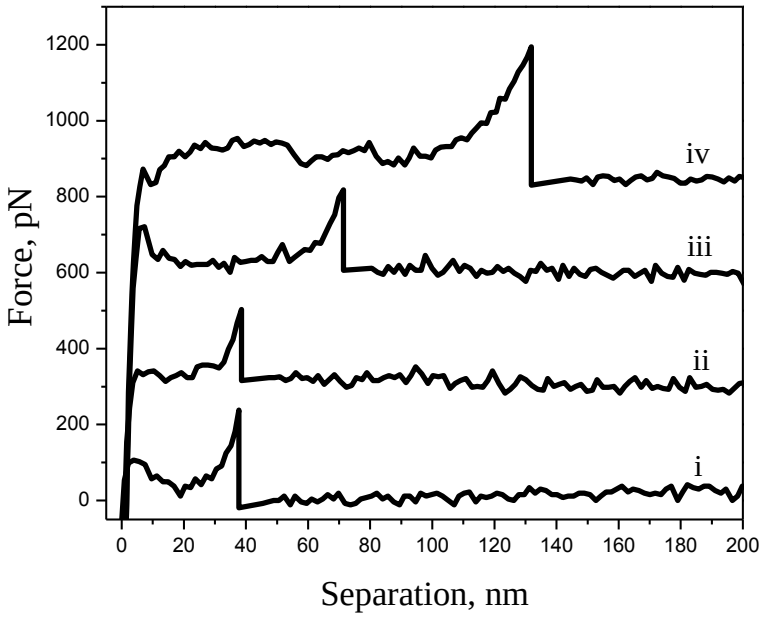

Figure 4.2 Representative force curves for the SP-A/DPPC interaction in the presence of Ca^{2+}. The force curves show different magnitudes of rupture forces and rupture lengths. Force curve (i) showed a greater unbinding force than (ii) but both showed similar rupture length. Force curve (iii) showed a longer rupture length but similar unbinding force as (i). Force curve (iv) showed the strongest interaction having the longest rupture length and largest unbinding force. For all the SP-A/lipid systems, >8000 force curves were collected to ensure a full statistical understanding of the interactions.

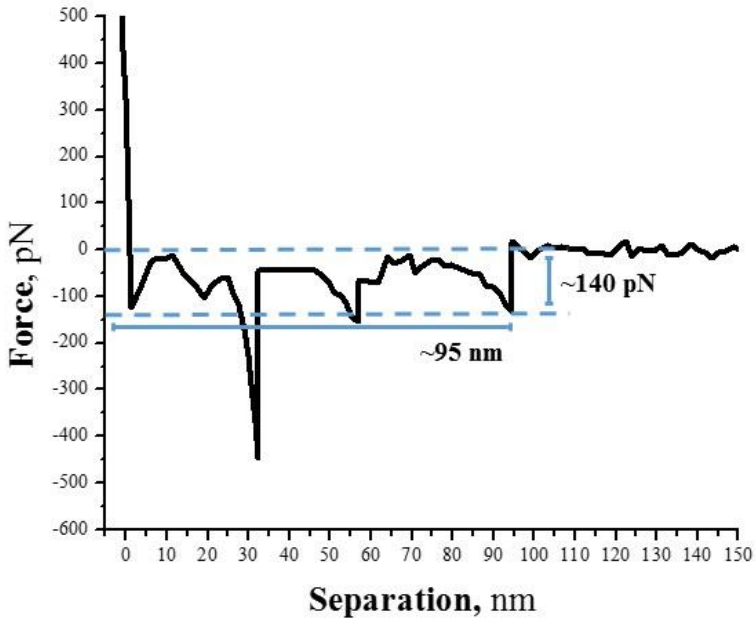

Figure 4.3 Representative force curve that exhibits multiple peaks. For such curves, only the final rupture peak was considered for the unbinding force values.

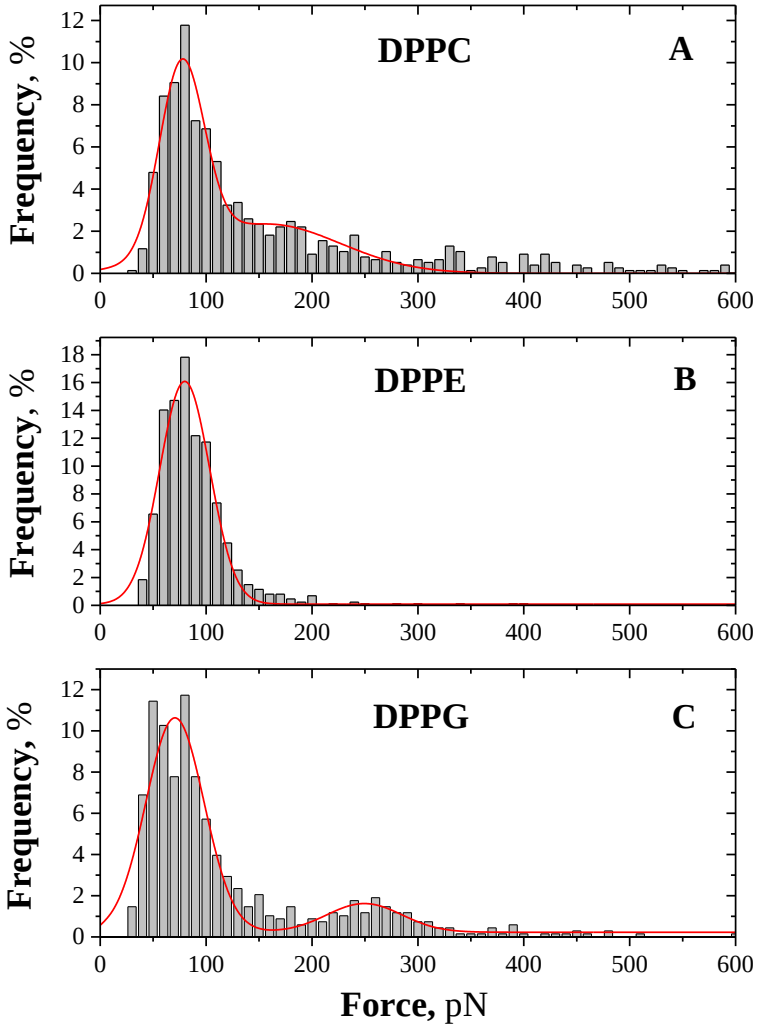

Figure 4.4 Frequency distribution of the unbinding forces for the interactions of SP-A in the presence of Ca^{2+} with (A) DPPC, (B) DPPE, and (C) DPPG in PBS buffer. The experimental data (gray bars) are fitted with a multi-Gaussian function (red line). The maximum peak forces from the Gaussian fit are reported in Table 4.1.

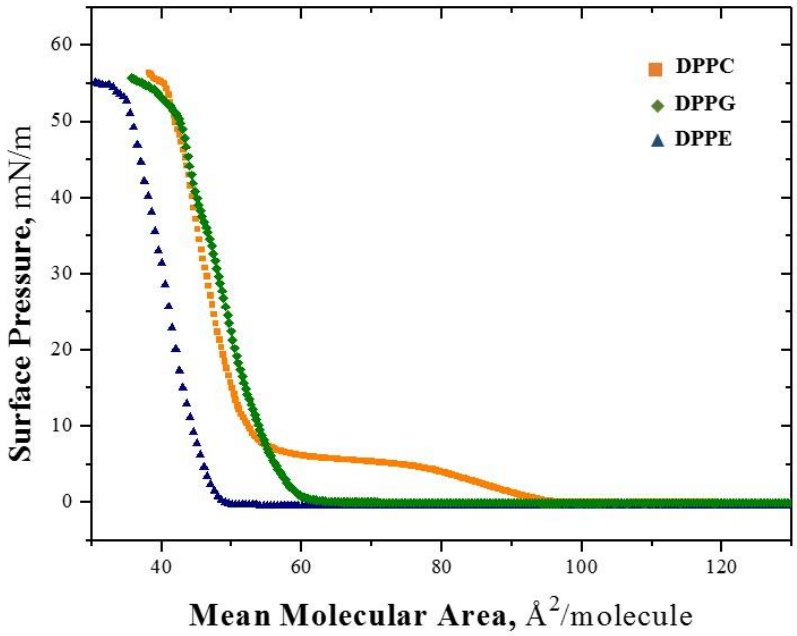

Figure 4.5 Surface-area isotherms of DPPC, DPPG and DPPE at ambient temperature. The LB film for each lipid were taken in the LC phase at surface pressures of 40 mN/m for DPPC, and 30 mN/m for both DPPG and DPPE.

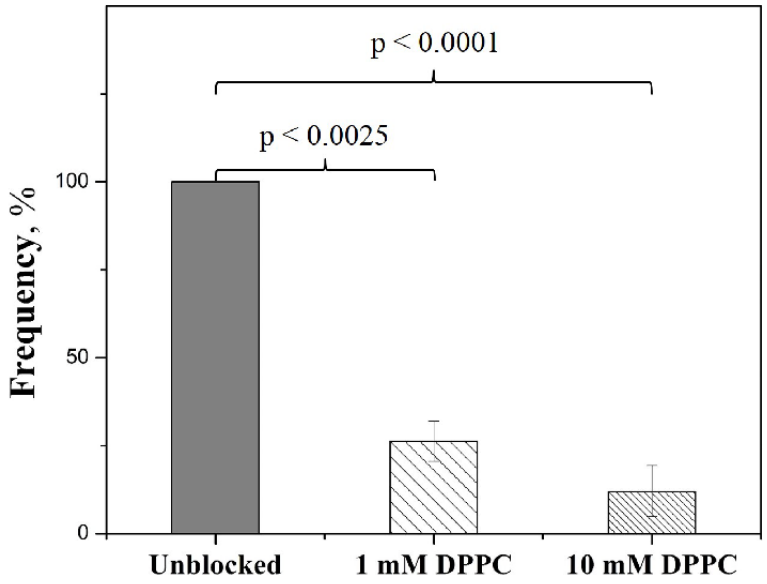

Figure 4.6 The SP-A/DPPC system was used for the DPPC blocking control experiment. The frequencies were normalized to show a relative decrease in frequency. There is a decrease of binding frequency to ~26% after addition of 1 mM DPPC in buffer and to ~12% after addition of 10 mM DPPC. The decrease in frequency after blocking confirms the specificity of interaction. The error bars represent the standard error from four repeated control experiments.

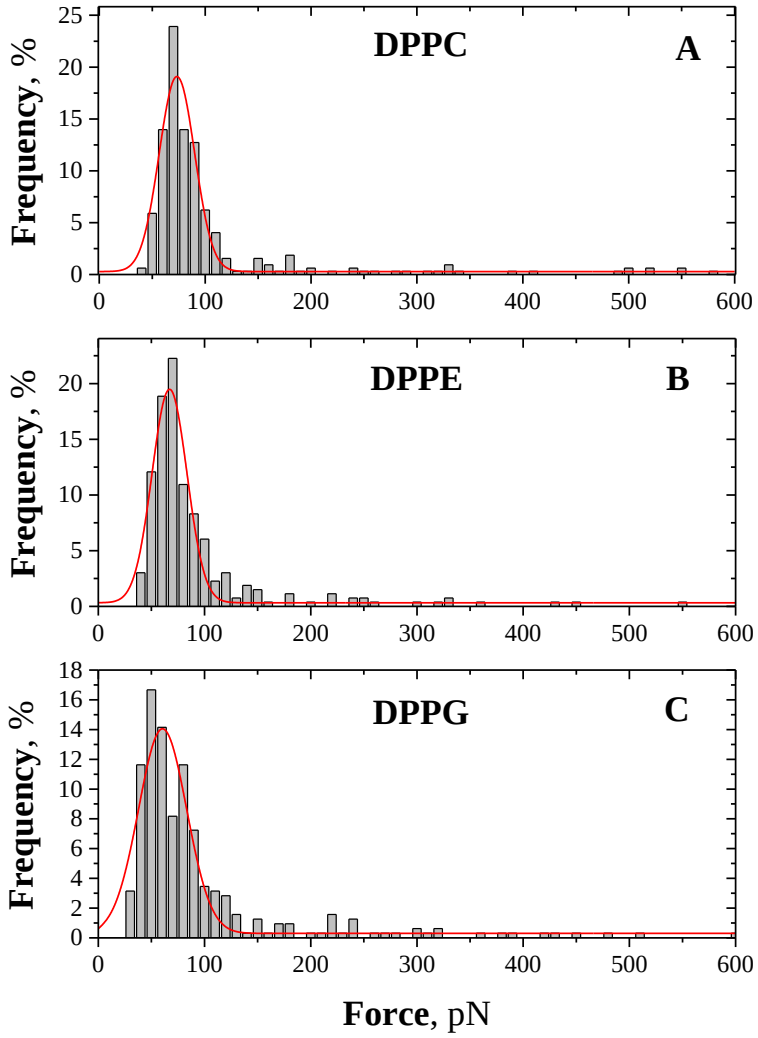

Figure 4.7 Control experiments: Frequency distribution of the unbinding forces for the interactions of SP-A in the absence of Ca^{2+} with (A) DPPC and (B) DPPE in PBS buffer with 1 mM SO_4^{2-}, and with (C) DPPG in PBS buffer only. The experimental data (gray bars) are fitted with a multi-Gaussian function (red line). The maximum peak forces from the Gaussian fit are reported in Table 4.2.

Chapter 5 : Determination of Dissociation Rate Constant (K_{OFF})

Force spectroscopy provides information on the nature of a ligand-receptor bond and its unbinding mechanism. In this part of the study, the dissociation rate constant for each SP-A/lipid systems in the presence of Ca^{2+}, to promote lipid binding, is experimentally calculated using the Bell-Evans model. The Bell-Evans method has been used extensively in characterizing binding interactions between molecules in vitro and in living cells.[86,110,111] By extrapolating the force to zero, the dissociation rate constant in the absence of an applied force (unstressed K_{off}) can be determined. According to Bell-Evans theory of kinetic bond rupture,[73,89,112] the force acting on a single receptor-ligand bond should depend on the natural logarithm of the loading rate of the bond as shown in Eqn. (2-3).

By probing the unbinding forces (F) over a range of loading rates (r), a dynamic force spectrum can be generated from which the parameters describing the energy landscape of the bond can be extracted. The bond loading rate (pN/s) is determined by multiplying the effective spring constant (K_{eff}) in pN/μm with the cantilever retraction speed (v) in μm/s:

$$r = vK_{eff} \tag{5-1}$$

K_{eff} approximates the effective spring constant of the cantilever-protein-lipid system. Because the bonds exist in different thermal states during bond rupture, a distribution of rupture forces is obtained for each loading rate. To generate the dynamic force spectrum, the most probable rupture force is taken for each loading rate value.[113,114] The most probable unbinding force (F) is then plotted against r and fitted with a logarithmic function:

$$F = \frac{K_B T}{X_\beta} \ln(r) + \frac{K_B T}{X_\beta} \ln(\frac{X_\beta}{K_{off} K_B T}) \tag{5-2}$$

where X_β is the position of the transition state and K_B is the Boltzmann constant. Eqn. (5.2) is another form of the Bell-Evan's equation (Eqn. (2-3)). The slope (m) permits calculation of X_β:

$$X_\beta = \frac{K_B T}{m} \tag{5-3}$$

where $K_B T \approx 4.1$ pN·nm at room temperature. The K_{off} can then be obtained by using the slope m and the y-intercept (b) of Eqn. (5-2):

$$K_{off} = \frac{1}{m} \exp(-\frac{b}{m}) \tag{5-4}$$

The bond lifetime can then be calculated:

$$\tau = \frac{1}{K_{off}} \tag{5-5}$$

The dynamic force spectrum for each SP-A/lipid system in this study is shown in Figure 5.1. The force spectrum for SP-A/DPPC and SP-A/DPPG interactions showed two distinct linear regimes, which locates two energy barriers along their unbinding pathway as shown by Evans and Ritchie.[51] For the SP-A/DPPE interaction however, the data did not show a clear linear dependence with the loading rate and thus the Bell-Evans model could not be fitted.

The parameters extracted from the force dynamic spectrum of each protein-lipid systems are listed in Table 5.1 and 5.2. The low strength regime presented low correlation values ($r^2 < 0.1$) suggesting that this region could not be modeled with the Bell-Evans theory. The parameters extracted from the low force regime also showed high uncertainties making it difficult to interpret the results. The high strength regime however, resulted in a clear linear dependence of the rupture force with the loading rate. Because of the distribution of rupture forces for each loading rate, the Bell-Evans equation was fitted for DPPC and DPPG's dynamic force spectrum over two different loading rate ranges for the high and low force regimes (Figure 5.1 A and B). Figure 5A shows similar number of data points for the low and high force regime. Low rupture force values were included for high loading rates in the high force regime. For Figure 5B, the higher force regime only included the rupture forces that showed a clear linear

dependence with the loading rate. The high strength regime K_{off} is generally reported because this dominates the kinetics of unbinding as it describes the rate-determining step.[115,116] Using the fitting range shown in Figure 5A, the K_{off} values calculated for the high-strength regime are 262.3 ± 1.4 s^{-1} and 270.3 ± 6.5 s^{-1} for DPPC and DPPG, respectively. For Figure 5B, K_{off} values of 78.9 ± 19.9 s^{-1} for DPPC and 189.9 ± 82.5 s^{-1} for DPPG were calculated. Both fitting approach resulted in a stronger interaction of DPPC with SP-A (lower K_{off}). The fitting range used for Figure 5B however showed a significant difference in the binding strength between DPPC and DPPG.

The bimodal character of DPPC and DPPG's force histograms (Figure 4.4) suggests the occurrence of two types of interactions (i.e., electrostatic and hydrophobic) between SP-A and DPPC and DPPG. These two interactions can also be assigned to the two different regimes (high and low force values) of the dynamic force spectrum plots. In the case of DPPE, the forces measured were mostly concentrated at the lower strength region as shown in Figure 5.1B. This result is consistent to the distinctive result of DPPE's histogram shown in Figure 4.4. From the histogram, SP-A/DPPE interaction revealed a narrow distribution of forces compared to the bimodal distributions of DPPC and DPPG. This unique result of DPPE may also be reflected in its dynamic force plot as most of the forces measured were observed at the lower force region (low loading rates). The Bell-Evans equation was not fitted to DPPE's force plot and the corresponding parameters were not extracted because the rupture forces measured did not show a clear linear dependence with the loading rate. At higher loading rates, however there is a linear

dependence of rupture force as seen in the cases for DPPC and DPPG (Figure 5.1A). It is also possible that the loading rates used for this study to measure the forces were not broad enough to probe a potential higher strength regime of SP-A/DPPE interaction. The lack of secondary interaction for DPPE as discussed in Chapter 4 can be due to the closer packing of the DPPE bilayer that could restrict the efficient penetration of SP-A and minimize hydrophobic interactions. This result also confirms the role of hydrophobic interactions on the binding strength of SP-A with the surfactant lipids.

From the K_{off} values obtained, the binding strength between SP-A and the three surfactant lipids follows in the order of DPPC > DPPG > DPPE. DPPC showed the strongest binding interaction with SP-A. This is consistent with the results from Chapter 4, considering the overall distribution of forces, wherein DPPC showed the strongest interaction. This is also consistent with studies that have shown stronger interaction of SP-A with DPPC compared to other surfactant lipids.

Figure 5.2 is an attempt to sketch the potential energy curves for each SP-A/DPPC and SP-A/DPPG interaction based from the parameters calculated in Tables 5.1 and 5.2. For DPPC and DPPG, the two linear regimes in their force spectrum plot locate two energy barriers in their potential energy curves. The high-strength regimes locate the inner barrier at X_β = 0.4 and 0.6 Å for DPPC and DPPG, respectively. The lower strength regimes map out the energy barriers at X_β = 3.0 and 4.6 Å, respectively. Extrapolation of each linear regime to zero force yields K_{off} and therefore the lifetime of the bond, τ.

Although the bond lifetimes for the inner barriers of DPPC and DPPG are similar, SP-A/DPPC interaction showed a slightly steeper energy barrier indicating that it can withstand higher forces than SP-A/DPPG interaction. DPPC however showed a brittle character as it can withstand high forces but small deformations (smaller X_β). DPPG showed an elastic character, as it can withstand lower forces but larger deformations (larger X_β).[115]

The K_{off} values obtained from the SP-A protein/lipid systems from this study are higher than the K_{off} values obtained for other protein-lipid systems. Garcia et al. reported K_{off} values of 10^{-2} s^{-1} for the interaction of DPPC and DPPG bilayers with a peripheral membrane binding protein, calgranulin C, using surface plasmon resonance.[117] The interaction of Raf-C1 protein, a member of the protein kinase family, with supported PG lipid bilayers revealed a K_{off} value of 10^{-4} s^{-1} using quartz crystal microbalance.[118] Walther et al. reported a K_{off} value of 10^{-3} s^{-1} for the adhesion of Mini-B protein, a synthetic surfactant related to native surfactant protein-B (SP-B), to DPPC liposomes using plasmon resonance.[119] The dissociation rate constants obtained under equilibrium conditions are often magnitudes lower than the dissociation rate constants obtained under dynamic conditions or in the presence of applied force.[73,113] Depending on the forces a system experiences in its physiological condition, the lifetime of the bonds may differ greatly between the experimental and physiological conditions. As mentioned in Chapter 4, the dynamic conditions of this experiment is a good model of the SP-A/lipid

interactions because of the shear forces experienced by SP-A in the alveolar space during the expansion and contraction of the lungs.

Protein-protein systems have been the commonly used ligand-receptor pair in force spectroscopy to study protein-protein interactions in the cellular level. Using similar loading rates as in this study, Evans et al reported a K_{off} value of 10^2 s^{-1} for a L-selectin/P-selectin glycoprotein ligand-1 (PSGL-1) interaction.[116] Merkel et al and Lee et al reported a K_{off} of 10^1 s^{-1} for an avidin/biotin interaction and fibrinogen/RGD linear peptide sequence, respectively.[112] The K_{off} values obtained in this study showed comparable values with these protein-protein systems using force spectroscopy. The SP-A/lipid systems however, still showed weaker interactions than other protein/protein systems.

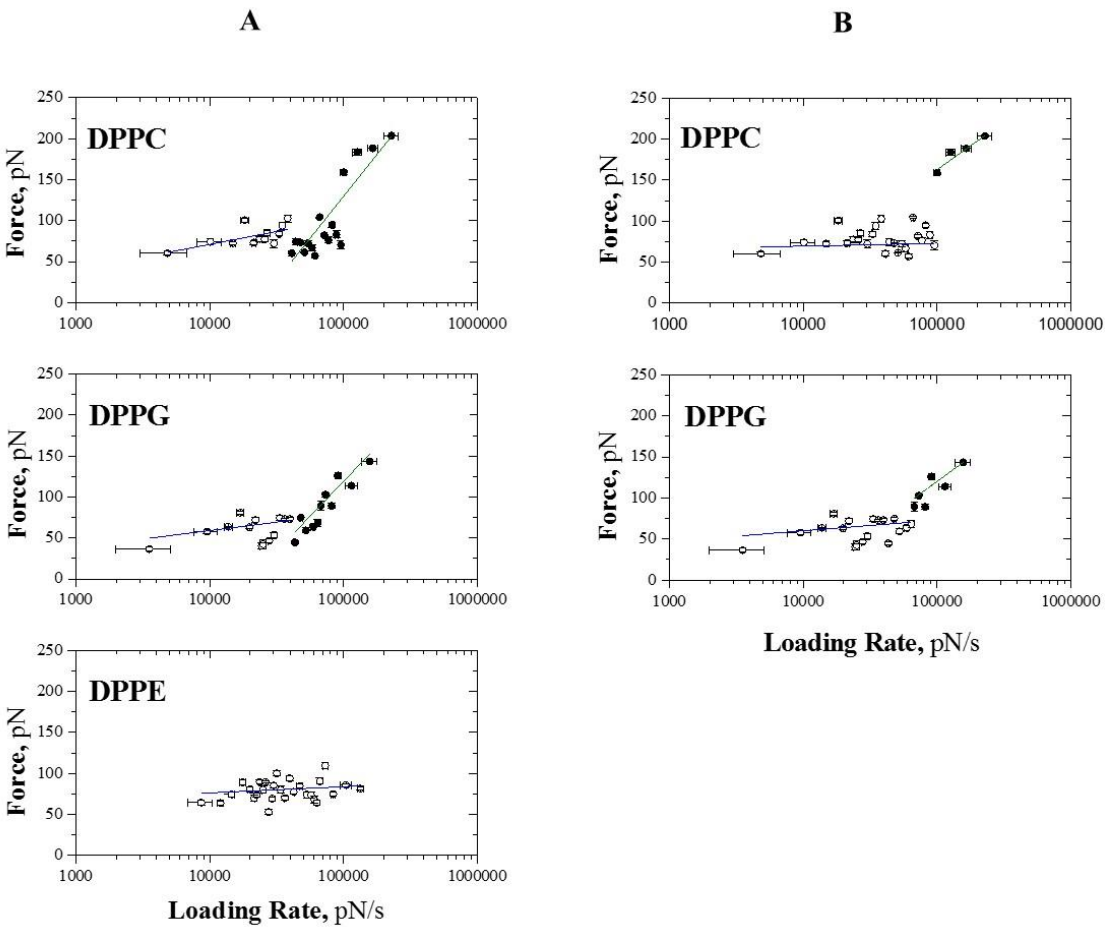

Figure 5.1 Force dynamic spectrum for each SP-A/lipid interaction. K_{off} values were calculated using the same fitting method over two different loading rate ranges. (A) Low force regime range is 10^3 - 10^4 pN/s and high force regime is 10^4 – 10^6 pN/s (B) Low force regime is 10^3 – 10^5 pN/s and high force regime range is 10^5-10^6 pN/s. Unbinding forces for DPPE did not show a clear linear dependence with loading rate and thus was not fitted with the Bell-Evans model.

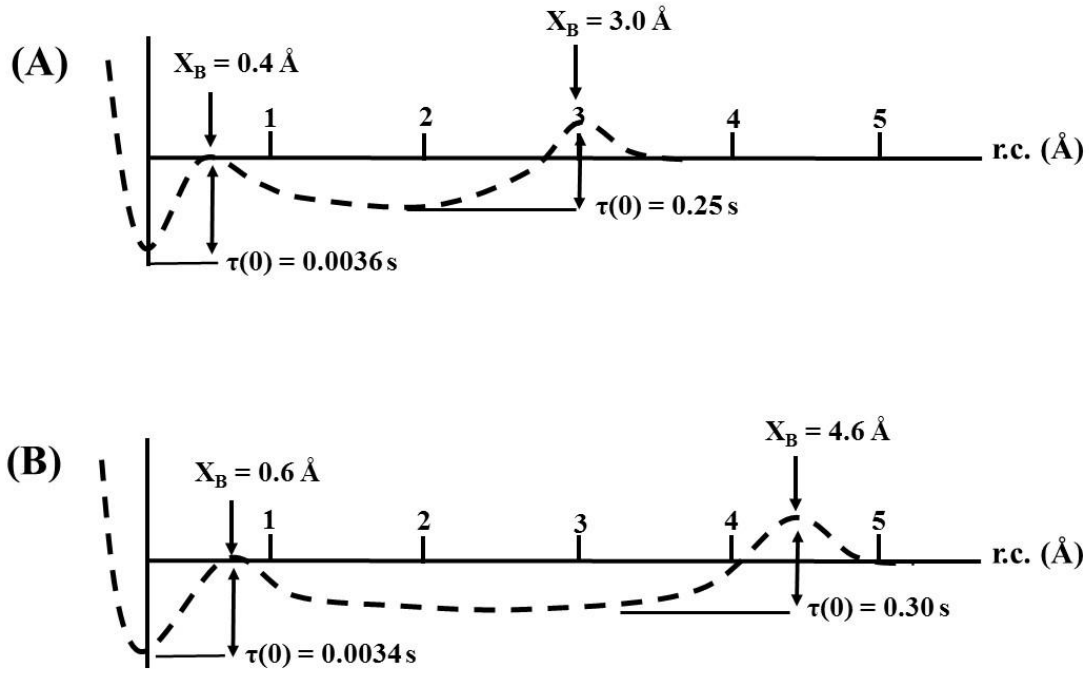

Figure 5.2 Potential energy curves for SP-A/DPPC (A) and SP-A/DPPG (B) interactions based from the parameters calculated from Figure 5.1A using the Bell-Evans model.

	Slope (m)	y-intercept (b)	X_β (Å)	K_{off} (s^{-1})	τ (s)
DPPC	13.6	-54.7	3.0 ± 0.1	4.0 ± 3.0	0.25 ± 0.14
DPPG	9.0	-23.9	4.6 ± 0.8	1.6 ± 1.8	0.30 ± 0.12

Table 5.1 Parameters extracted from the low strength regime of the dynamic force spectrum plot in Figure 5.1A using Bell-Evans model for each SP-A/lipid system. The unbinding force values in the low strength regime of Figure 5.1B did not show a clear linear dependence with the loading rate and hence was not fitted with the Bell-Evans equation.

	A					B				
	Slope (m)	**y-intercept (b)**	**X_β (Å)**	**K_{off} (s^{-1})**	**τ (s)**	**Slope (m)**	**y-intercept (b)**	**X_β (Å)**	**K_{off} (s^{-1})**	**τ (s)**
DPPC	88.9	-893.6	0.4 ± 0.0	262.3 ± 1.4	0.0036 ± 0.0000	50.4	-417.8	0.08 ± 0.01	78.9 ± 19.9	0.012 ± 0.004
DPPG	73.9	-731.8	0.6 ± 0.1	270.4 ± 6.5	0.0034 ± 0.0000	51.8	-476.3	0.08 ± 0.02	189.9 ± 82.5	0.005 ± 0.002

Table 5.2 Parameters extracted from the high strength regime of the dynamic force spectrum plot in Figure 5.1A and B using Bell-Evans model for each SP-A/lipid system.

Chapter 6 : Conclusions and Future Work

The work presented in this thesis is motivated by an interest in understanding the role of SP-A in lung surfactant activity and phospholipid metabolism which is dependent upon its ability to bind to surfactant lipids. Lipid binding studies done on SP-A are in equilibrium conditions, but due to the conditions in the lungs during the breathing cycle, it is best to study the lipid binding properties of SP-A under dynamic conditions. In this study, AFM was used to quantify the distribution of unbinding forces between SP-A and three surfactant lipids under dynamic conditions. The SP-A-coated tip and SLBs were used to model the dynamic conditions of SP-A/lipid binding in the alveolar hypophase. DPPC, being the most abundant alveolar phospholipid, showed a broader force distribution among the three phospholipids that were studied. Although DPPC revealed a comparable main force value as DPPE for the SP-A/lipid headgroup interaction, its broad and bimodal distribution of forces indicates a secondary interaction resulting mainly from hydrophobic interactions of the lipid acyl chains with the protein. These forces resulted in an overall preferred and stronger interaction of SP-A for DPPC.

To verify the role of the lipid headgroup charge on the main unbinding force through electrostatic interactions, control experiments were done in the absence of Ca^{2+}. DPPC and DPPE experiments done in the absence of Ca^{2+} and in the presence of SO_4^{2-} resulted in a decrease in the main unbinding force which suggests the partial shielding and the

role of the positive charge of the lipid headgroup in electrostatic interactions with SP-A. In the case of SP-A/DPPG interaction in the absence of Ca^{2+}, a decrease in the main unbinding force and distribution of force was also observed indicating the Ca^{2+} dependent binding with SP-A. These set of control experiments shows the role of electrostatic interactions in SP-A/lipid binding. By shielding the positive charge of DPPC and DPPE and unshielding the negative charge of DPPG, a decrease in the main peak force and overall distribution of unbinding forces is observed which can confirm the contribution of electrostatic interactions on the main peak unbinding force.

To further evaluate the strength of interaction, the dissociation constants for each protein-lipid systems were determined using the Bell-Evans model. The two Gaussian peaks observed for DPPC and DPPG histograms corresponded to two linear regimes in their force spectrum plot. The K_{off} value was not determined for DPPE as the forces measured did not exhibit clear dependence with the loading rate. The dissociation rate constants revealed strongest binding strength for SP-A/DPPC interaction. The two types of interactions, as suggested by the bimodal distribution of force for the DPPC and DPPG histograms, were also observed in their force spectrum plots. The two modes of binding can be from electrostatic interactions between the charged lipid headgroup and SP-A and hydrophobic interactions between the lipid acyl chains and SP-A. Hydrophobic interactions are assigned to higher forces measured and these forces gave a strong dependence with the loading rate wherein K_{off} is extracted.

The overall results suggest that SP-A/lipid interaction involves both electrostatic and hydrophobic interactions and that both should be taken into account in evaluating the strength of interaction of lipids with SP-A. Electrostatic interactions between the charged lipid headgroup and SP-A can orient the protein for a more favorable interaction with the lipids. As suggested by previous studies, hydrophobic interaction may be the primary mode of binding of SP-A with surfactant lipids and that it has a strong binding with DPPC compared to other surfactant phospholipids. This is also observed in this study wherein DPPC presented the broadest overall distribution of force which takes into account both electrostatic and hydrophobic interactions. The dissociation rate constant also revealed a stronger interaction of SP-A with DPPC than DPPG or DPPE.

Further work should be done to probe the changes in the SP-A/lipid interactions under different conditions. Change in temperature, pH and ionic concentration are among the important conditions that must be explored to fully understand the binding interactions of SP-A with different surfactant lipids. The effect of the physical state of the phospholipid bilayer in the unbinding forces is also of interest.

References

1. Daniels, C. B., and Orgeig, S. *News in Physiological Sciences* **2003**, 18, 151-157.
2. Notter, R. H. (2000) *Lung Surfactants: Basic Science and Clinical Applications*, Marcel Dekker, Inc., New York.
3. Schurch, S., Lee, M., and Gehr, P. *Pure Appl. Chem.* **1992**, 64, 1745-1750.
4. Klein, J. M., McCarthy, T. A., Dagle, J. M., and Snyder, J. M. *Am. J. Physiol.: Lung Cell. Mol. Physiol.* **2002**, 282, L386-L393.
5. Williams, M. C. *J. Cell Biol.* **1977**, 72, 260-277.
6. Malloy, J. L., and Wright, J. R. *Respir. Res.* **2004**, 5, 1-9.
7. Veldhuizen, R., Nag, K., Orgeig, S., and Possmayer, F. *Biochim. Biophys. Acta, Mol. Basis Dis.* **1998**, 1408, 90-108.
8. Perez-Gil, J., and Weaver, T. E. *Physiology.* **2010**, 25, 132-141.
9. Zuo, Y. Y., Veldhuizen, R. A. W., Neumann, A. W., Petersen, N. O., and Possmayer, F. *Biochim. Biophys. Acta, Biomembr.* **2008**, 1778, 1947-1977.
10. Kuronuma, K., Mitsuzawa, H., Takeda, K., Nishitani, C., Chan, E. D., Kuroki, Y., Nakamura, M., and Voelker, D. R. *J. Biol. Chem.* **2009**, 284, 25488-25500.
11. Casals, C. *Pediatr. Pathol. Mol. Med.* **2001**, 20, 249-268.
12. Hawgood, S., Efrati, H., Schilling, J., and Benson, B. J. *Biochem. Soc. Trans.* **1985**, 13, 1092-1096.
13. Khubchandani, K. R., and Snyder, J. M. *FASEB J.* **2001**, 15, 59-69.
14. Sueishi, K., and Benson, B. J. *Biochim. Biophys. Acta* **1981**, 665, 442-453.
15. Taneva, S., McEachren, T., Stewart, J., and Keough, K. M. W. *Biochemistry.* **1995**, 34, 10279-10289.
16. Voss, T., Eistetter, H., Schafer, K. P., and Engel, J. *J. Mol. Biol.* **1988**, 201, 219-227.
17. Creuwels, L., vanGolde, L. M. G., and Haagsman, H. P. *Lung* **1997**, 175, 1-39.
18. Haagsman, H. P., White, R. T., Schilling, J., Lau, K., Benson, B. J., Golden, J., Hawgood, S., and Clements, J. A. *Am. J. Physiol.* **1989**, 257, L421-L429.
19. Benne, C. A., Kraaijeveld, C. A., Vanstrijp, J. A. G., Brouwer, E., Harmsen, M., Verhoef, J., Vangolde, L. M. G., and Vaniwaarden, J. F. *J. Iinfect. Dis.* **1995**, 171, 335-341.
20. Haagsman, H. P., Elfring, R. H., Vanbuel, B. L. M., and Voorhout, W. F. *Biochem. J* **1991**, 275, 273-276.
21. Vaniwaarden, J. F., Vanstrijp, J. A. G., Visser, H., Haagsman, H. P., Verhoef, J., and Vangolde, L. M. G. *J. Biol. Chem.* **1992**, 267, 25039-25043.
22. King, R. J., Phillips, M. C., Horowitz, P. M., and Dang, S. C. *Biochim. Biophys. Acta* **1986**, 879, 1-13.
23. McCormack, F. X., Calvert, H. M., Watson, P. A., Smith, D. L., Mason, R. J., and Voelker, D. R. *J. Biol. Chem.* **1994**, 269, 5833-5841.

24. Meyboom, A., Maretzki, D., Stevens, P. A., and Hofmann, K. P. *J. Biol. Chem.* **1997**, 272, 14600-14605.
25. Meyboom, A., Maretzki, D., Stevens, P. A., and Hofmann, K. P. *Biochim. Biophys. Acta, Mol. Cell Biol. Lipids.* **1999**, 1441, 23-35.
26. Reilly, K. E., Mautone, A. J., and Mendelsohn, R. *Biochemistry* **1989**, 28, 7368-7373.
27. Voorhout, W. F., Veenendaal, T., Haagsman, H. P., Verkleij, A. J., Vangolde, L. M. G., and Geuze, H. J. *J. Histochem. Cytochem.* **1991**, 39, 1331-1336.
28. Williams, M. C., Hawgood, S., and Hamilton, R. L. *Am. J. Respir. Cell Mol. Biol.* **1991**, 5, 41-50.
29. Ruano, M. L. F., Nag, K., Casals, C., Perez-Gil, J., and Keough, K. M. W. *Biophys. J.* **1999**, 77, 1469-1476.
30. Ruano, M. L. F., Nag, K., Worthman, L. A., Casals, C., Perez-Gil, J., and Keough, K. M. W. *Biophys. J.* **1998**, 74, 1101-1109.
31. Kuroki, Y., and Akino, T. *J. Biol. Chem.* **1991**, 266, 3068-3073.
32. Hawgood, S., Benson, B. J., and Hamilton, R. L. *Biochemistry.* **1985**, 24, 184-190.
33. King, R. J., Carmichael, M. C., and Horowitz, P. M. *J. Biol. Chem.* **1983**, 258, 672-680.
34. Perez-Gil, J. *Biochim. Biophys. Acta, Biomembr.* **2008**, 1778, 1676-1695.
35. Ruano, M. L. F., Miguel, E., PerezGil, J., and Casals, C. *Biochem. J* **1996**, 313, 683-689.
36. Casals, C., Miguel, E., and Perez-Gil, J. *Biochem. J* **1993**, 296, 585-593.
37. Kuroki, Y., McCormack, F. X., Ogasawara, Y., Mason, R. J., and Voelker, D. R. *J. Biol. Chem.* **1994**, 269, 29793-29800.
38. McCormack, F. X., Kuroki, Y., Stewart, J. J., Mason, R. J., and Voelker, D. R. *J. Biol. Chem.* **1994**, 269, 29801-29807.
39. McCormack, F. X., Stewart, J., Voelker, D. R., and Damodarasamy, M. *Biochemistry.* **1997**, 36, 13963-13971.
40. Ogasawara, Y., and Voelker, D. R. *J. Biol. Chem.* **1995**, 270, 14725-14732.
41. Seaton, B. A., Crouch, E. C., McCormack, F. X., Head, J. F., Hartshorn, K. L., and Mendelsohn, R. *Innate Immunity* **2010**, 16, 143-150.
42. Ogasawara, Y., McCormack, F. X., Mason, R. J., and Voelker, D. R. *J. Biol. Chem.* **1994**, 269, 29785-29792.
43. Sano, H., Kuroki, Y., Honma, T., Ogasawara, Y., Sohma, H., Voelker, D. R., and Akino, T. *J. Biol. Chem.* **1998**, 273, 4783-4789.
44. Wright, J. R. *Am. J. Physiol.* **1990**, 259, L1-L12.
45. Wright, J. R., and Youmans, D. C. *Am. J. Physiol.: Lung Cell. Mol. Physiol.* **1995**, 268, L772-L780.
46. Pison, U., Wright, J. R., and Hawgood, S. *Am J. Physiol.* **1992**, 262, L412-L417.
47. Poelma, D. L. H., Zimmermann, L. J. I., Scholten, H. H., Lachmann, B., and van Iwaarden, J. F. *Am. J. Physiol.: Lung Cell. Mol. Physiol.* **2002**, 283, L648-L654.
48. Wright, J. R., Borchelt, J. D., and Hawgood, S. *Proc. Natl. Acad. Sci. USA.* **1989**, 86, 5410-5414.

49. Worthman, L. A. D., Nag, K., Rich, N., Ruano, M. L. F., Casals, C., Perez-Gil, J., and Keough, K. M. W. *Biophys. J.* **2000**, 79, 2657-2666.
50. Lee, C. K., Wang, Y. M., Huang, L. S., and Lin, S. M. *Micron.* **2007**, 38, 446-461.
51. Evans, E., and Ritchie, K. *Biophys. J.* **1997**, 72, 1541-1555.
52. Eibl, R. H., and Moy, V. T. (2005) Atomic Force Microscopy Measurements of Protein–Ligand Interactions on Living Cells. in *Methods in Molecular Biology* (Nienhaus, G. U. ed.), Humana Press Inc., Totowa, NJ. pp 439-449
53. Helenius, J., Heisenberg, C. P., Gaub, H. E., and Muller, D. J. *J. Cell Sci.* **2008**, 121, 1785-1791.
54. Desmeules, P., Grandbois, M., Bondarenko, V. A., Yamazaki, A., and Salesse, C. *Biophys. J.* **2002**, 82, 3343-3350.
55. Cross, B., Ronzon, F., Roux, B., and Rieu, J. P. *Langmuir.* **2005**, 21, 5149-5153.
56. Thormann, E., Dreyer, J. K., Simonsen, A. C., Hansen, P. L., Hansen, S., Holmskov, U., and Mouritsen, O. G. *Biochemistry.* **2007**, 46, 12231-12237.
57. Floros, J., Steinbrink, R., Jacobs, K., Phelps, D., Kriz, R., Recny, M., Sultzman, L., Jones, S., Taeusch, H. W., Frank, H. A., and Fritsch, E. F. *J. Biol. Chem.* **1986**, 261, 9029-9033.
58. White, R. T., Damm, D., Miller, J., Spratt, K., Schilling, J., Hawgood, S., Benson, B., and Cordell, B. *Nature* **1985**, 317, 361-363.
59. Head, J. F., Mealy, T. R., McCormack, F. X., and Seaton, B. A. *J. Biol. Chem.* **2003**, 278, 43254-43260.
60. Binnig, G., Quate, C. F., and Gerber, C. *Phys. Rev. Lett.* **1986**, 56, 930-933.
61. D'Acunto, M. (2006) Nanotribology and Biomaterials: New Challenges for Atomic Force Microscopy. in *Nanophysics, Nanoclusters and Nanodevices* (Gehar, K. S. ed.), Nova Publishers, Inc., New York. pp
62. Seo, Y., and Jhe, W. *Rep. Prog. Phys.* **2008**, 71,
63. Butt, H. J., Cappella, B., and Kappl, M. *Surf. Sci. Rep.* **2005**, 59, 1-152.
64. Corporation, O. (2014) Low-Wear Silicon Nitride Cantilever.
65. (2004) *Atomic Force Microscopy: Biomedical Methods and Applications*, Humana Press, Totowa, New Jersey
66. Cappella, B., and Dietler, G. *Surf. Sci. Rep.* **1999**, 34, 1-+.
67. Noy, A., and Friddle, R. W. *Methods* **2013**, 60, 142-150.
68. Berquand, A., and Ohler, B. (2010) Common Approaches to Tip Functionalization for AFM-Based Molecular Recognition Measurements. (Bruker ed.
69. Hutter, J. L., and Bechhoefer, J. *Rev. Sci. Instrum.* **1993**, 64, 1868-1873.
70. Butt, H. J., and Jaschke, M. *Nanotechnology* **1995**, 6, 1-7.
71. Levy, R., and Maaloum, M. *Nanotechnology* **2002**, 13, 33-37.
72. Viani, M. B., Schaffer, T. E., Chand, A., Rief, M., Gaub, H. E., and Hansma, P. K. *J. Appl. Phys.* **1999**, 86, 2258-2262.
73. Evans, E. *Annu. Rev. Biophys. Biomol. Struct.* **2001**, 30, 105-128.
74. Friddle, R. W., Noy, A., and De Yoreo, J. J. *Proc. Natl. Acad. Sci. USA.* **2012**, 109, 13573-13578.

75. DeRose, J. A., and Revel, J. P. *Thin Solid Films* **1998**, 331, 194-202.
76. Jandt, K. D., McMaster, T. J., Miles, M. J., and Petermann, J. *Macromolecules* **1993**, 26, 6552-6556.
77. Klinov, D. V., Lagutina, I. V., Prokhorov, V. V., Neretina, T., Khil, P. P., Lebedev, Y. B., Cherny, D. I., Demin, V. V., and Sverdlov, E. D. *Nucleic Acids Res.* **1998**, 26, 4603-4610.
78. Orisaka, S., Minobe, T., Uchihashi, T., Sugawara, Y., and Morita, S. *Appl. Surf. Sci.* **1999**, 140, 243-246.
79. Hansma, H. G., Oroudjev, E., Baudrey, S., and Jaeger, L. *J. Microsc-Oxford* **2003**, 212, 273-279.
80. Li, S. L., and Palmer, A. F. *Langmuir* **2004**, 20, 7917-7925.
81. Reddy, C. V. G., Malinowska, K., Menhart, N., and Wang, R. *Biochim. Biophys. Acta, Biomembr.* **2004**, 1667, 15-25.
82. Sitko, J. C., Mateescu, E. M., and Hansma, H. G. *Biophys. J.* **2003**, 84, 419-431.
83. Chen, A., and Moy, V. T. *Biophys. J.* **2000**, 78, 2814-2820.
84. Kaur, J., Singh, K. V., Schmid, A. H., Varshney, G. C., Suri, C. R., and Raje, M. *Biosens Bioelectron.* **2004**, 20, 284-293.
85. Kienberger, F., Kada, G., Mueller, H., and Hinterdorfer, P. *J. Mol. Biol.* **2005**, 347, 597-606.
86. Lee, I., and Marchant, R. E. *Surf. Sci.* **2001**, 491, 433-443.
87. Li, H. B., Zhang, W. K., Xu, W. Q., and Zhang, X. *Macromolecules* **2000**, 33, 465-469.
88. Rief, M., Clausen-Schaumann, H., and Gaub, H. E. *Nat. Struct. Biol.* **1999**, 6, 346-349.
89. Bell, G. *Science* **1978**, 200, 618-627.
90. Nevo, R., Stroh, C., Kienberger, F., Kaftan, D., Brumfeld, V., Elbaum, M., Reich, Z., and Hinterdorfer, P. *Nature Structural Biology* **2003**, 10, 553-557.
91. Leite, F. L., and Herrmann, P. S. P. *J. Adhes. Sci. Technol.* **2005**, 19, 365-405.
92. Beharka, A. A., Gaynor, C. D., Kang, B. K., Voelker, D. R., McCormack, F. X., and Schlesinger, L. S. *J. Immunol.* **2002**, 169, 3565-3573.
93. Crowther, J. E., Kutala, V. K., Kuppusamy, P., Ferguson, J. S., Beharka, A. A., Zweier, J. L., McCormack, F. X., and Schlesinger, L. S. *J. Immunol.* **2004**, 172, 6866-6874.
94. Crowther, J. E., and Schlesinger, L. S. *Am. J. Physiol.: Lung Cell. Mol. Physiol.* **2006**, 290, L334-L342.
95. Jr., O. N. O. *Braz. J. Phys.* **1992**, 22, 60-69.
96. Chen, X. K., Huang, Z. S., Hua, W., Castada, H., and Allen, H. C. *Langmuir.* **2010**, 26, 18902-18908.
97. Baumgartner, W., Hinterdorfer, P., Ness, W., Raab, A., Vestweber, D., Schindler, H., and Drenckhahn, D. *Proc. Natl. Acad. Sci. USA.* **2000**, 97, 4005-4010.
98. Casillas-Ituarte, N. N., Lower, B. H., Lamlertthon, S., Fowler, V. G., and Lower, S. K. *J. Biol. Chem.* **2012**, 287, 6693-6701.

99. Schwesinger, F., Ros, R., Strunz, T., Anselmetti, D., Guntherodt, H. J., Honegger, A., Jermutus, L., Tiefenauer, L., and Pluckthun, A. *Proc. Natl. Acad. Sci. USA.* **2000**, 97, 9972-9977.
100. Strunz, T., Oroszlan, K., Schafer, R., and Guntherodt, H. J. *Proc. Natl. Acad. Sci. USA.* **1999**, 96, 11277-11282.
101. Bassereau, P., and Pincet, F. *Langmuir* **1997**, 13, 7003-7007.
102. Benz, M., Gutsmann, T., Chen, N. H., Tadmor, R., and Israelachvili, J. *Biophys. J.* **2004**, 86, 870-879.
103. Mou, J. X., Yang, J., and Shao, Z. F. *J. Mol. Biol.* **1995**, 248, 507-512.
104. Boggs, J. M. *Can. J. Biochem.* **1980**, 58, 755-770.
105. Hitchcock, P. B., Mason, R., Thomas, K. M., and Shipley, G. G. *Proc. Natl. Acad. Sci. USA.* **1974**, 71, 3036-3040.
106. Leekumjorn, S., and Sum, A. K. *Biochim. Biophys. Acta, Biomembr.* **2007**, 1768, 354-365.
107. Boggs, J. M., Stollery, J. G., and Moscarello, M. A. *Biochemistry* **1980**, 19, 1226-1234.
108. Stollery, J. G., Boggs, J. M., and Moscarello, M. A. *Biochemistry* **1980**, 19, 1219-1226.
109. Smith, R., and Tanford, C. *J. Mol. Biol.* **1972**, 67, 75-83.
110. Chang, M. I., Panorchan, P., Dobrowsky, T. M., Tseng, Y., and Wirtz, D. *J. Virol.* **2005**, 79, 14748-14755.
111. Alcaraz, J., Buscemi, L., Grabulosa, M., Trepat, X., Fabry, B., Farre, R., and Navajas, D. *Biophys. J.* **2003**, 84, 2071-2079.
112. Merkel, R., Nassoy, P., Leung, A., Ritchie, K., and Evans, E. *Nature* **1999**, 397, 50-53.
113. Franz, C. M., and Taubenberger, A. (2012) AFM-Based Single-Cell Force Spectroscopy. in *Atomic Force Microscopy in Liquid*, Wiley-VCH Verlag GmbH & Co. KGaA. pp 307-330
114. Zhang, X. H., Wojcikiewicz, E., and Moy, V. T. *Biophys. J.* **2002**, 83, 2270-2279.
115. Bustanji, Y., Arciola, C. R., Conti, M., Mandello, E., Montanaro, L., and Samori, B. *Proc. Natl. Acad. Sci. USA.* **2003**, 100, 13292-13297.
116. Evans, E., Leung, A., Hammer, D., and Simon, S. *Proc. Natl. Acad. Sci. USA.* **2001**, 98, 3784-3789.
117. Garcia, A. F., Lopes, J. L. S., Costa, A. J., Wallace, B. A., and Araujo, A. P. U. *Plos One* **2013**, 8,
118. Eing, A., Janshoff, A., Galla, H. J., Block, C., and Steinem, C. *Chembiochem* **2002**, 3, 190-197.
119. Walther, F. J., Waring, A. J., Hernandez-Juviel, J. M., Gordon, L. M., Schwan, A. L., Jung, C. L., Chang, Y. S., Wang, Z. D., and Notter, R. H. *Plos One* **2007**, 2,